Chapter 7
Electrodeposited Alloys and Multilayered Structures

7.1 Introduction

It is general experience in materials science that alloy can exhibit qualities that are unobtainable with parent metals. This is particularly true for electrodeposited alloys, mainly due to formation of metastable phases and intermediate layers. Some important properties of materials, such as hardness, ductility, tensile strength, Young's modulus, corrosion resistance, solderability, wear resistance, antifriction service, etc., may be enhanced. At the same time, some properties that are not characteristic for parent metals, such as high magnetic permeability, other magnetic and electrical properties, amorphous structure, etc., can also be obtained. In some cases, alloy coatings may be more suitable for subsequent electroplate overlayers and conversion chemical treatments [1].

Some alloys may be more easily obtained by electrodeposition than by metallurgical processes. This is particularly true for alloys composed of metals having large differences in melting temperatures or metals that cannot be mixed in a liquid state. Such metals can very often be codeposited from the solutions (e.g., alloys Ag–Ni, Ag–Co, and Cd–Co). Taking into account that some metals cannot be electrodeposited from the aqueous solutions (Ti, V, W, Nb, Zr, etc.), they could be electrodeposited from the melts of their salts. In recent times, the processes of metal and alloy electrodeposition from the room-temperature molten salts were also investigated and developed (cf. electrodeposition of Al–Cu, Al–Co, Al–Ni alloys from $AlCl_3$–MeEtImCl melt).

The fast-growing requirements of modern industry for materials with special qualities in the last century have given rise to increasing interest in electrodeposition of alloys, particularly in corrosion protection and in the modern electronic industry [1].

From 1842 until the end of the nineteenth century, over 180 alloys involving 40 elements have been electrodeposited [2]. An excellent review of the achievements up to 1962 is given in the book by Brenner [3], while from practical point of

K.I. Popov et al., *Morphology of Electrochemically and Chemically Deposited Metals*, DOI 10.1007/978-3-319-26073-0_7

view, it is recommended to consider the book of Bondar, Grimina, and Pavlov [4], which contains recipes and references for more than 1100 baths for alloy electrodeposition.

Concerning scientific approach of the electrodeposition of alloys, all the results obtained until 1995, mainly connected with the thermodynamics and kinetics of alloy electrodeposition, are summarized in the chapter by Despić and Jović [1] and Jović et al. [5]. In the present chapter, the morphology of electrodeposited alloys will be the main subject.

7.2 Electrodeposition of Alloys from Aqueous Solutions

7.2.1 Conditions for Electrodeposition of Alloys

The metals immersed in the solution of their simple salts establish the reversible potential. The values of the reversible potentials for different metals could differ for about 3 V. Electrodeposition of metals could take place only at potentials more negative than the reversible ones. Accordingly, in the solution of ions of two metals (cf. Cu^{2+} and Zn^{2+}) with one being on the positive side of the potential scale (vs. SHE) (Cu) and another one being on the negative side of the potential scale (Zn), intensive electrodeposition of Cu could take place at potentials at which Zn would not electrodeposit at all. Taking into account that the reversible potentials of metals could change with the presence of different anions in the solution (complexation of metal ions) and that the rates of electrodeposition of different metals are usually different, it is possible to achieve conditions for simultaneous electrodeposition of these two metals [1, 5].

For simultaneous electrodeposition of two metals, A and B, their electrodeposition potentials (E) must be identical, $E(\mathrm{A}) = E(\mathrm{B})$, i.e.,

$$E_\mathrm{r}(\mathrm{A}) + \eta(\mathrm{A}) = E_\mathrm{r}(\mathrm{B}) + \eta(\mathrm{B}) \tag{7.1}$$

where $E_\mathrm{r}(\mathrm{A})$ and $E_\mathrm{r}(\mathrm{B})$ are reversible potentials of metals A and B, while $\eta(\mathrm{A})$ and $\eta(\mathrm{B})$ correspond to the overpotentials needed for the electrodeposition of these two metals. The reversible potential could be changed by the change of metal ion concentration in the solution and by the temperature of the solution and is defined by the Nernst equation:

$$E_\mathrm{r}(\mathrm{A}) = E^\Theta(\mathrm{A}) + \frac{RT}{pF}\ln a(\mathrm{A}^{\mathrm{p}+}) \tag{7.2}$$

$$E_\mathrm{r}(\mathrm{B}) = E^\Theta(\mathrm{B}) + \frac{RT}{qF}\ln a(\mathrm{A}^{\mathrm{q}+}) \tag{7.3}$$

where E^{Θ}(A) and E^{Θ}(B) are standard potentials of metals A and B, a activities of corresponding metal ions in the solution, and p and q numbers of electrons to be exchanged during the process of metal electrodeposition.

The condition defined by Eq. (7.1) could be accepted only as a first approximation, since the potential of the metal electrodeposition is undefined quantity if the value of corresponding current density is not known. It appears that a better definition of the conditions for simultaneous electrodeposition of two metals would be current density (i) at which both metals electrodeposit with approximately the same current density. More precisely, for two-component alloy to be electrodeposited with the molar ratio of the more noble metal x and the less noble metal $(1-x)$, assuming that Faraday's law is obeyed, the following relations should be fulfilled:

$$x = \frac{n_A}{n_A + n_B} = \frac{\frac{i_A}{p}}{\frac{i_A}{p} + \frac{i_B}{q}} \tag{7.4}$$

and

$$(1-x) = \frac{n_B}{n_A + n_B} = \frac{\frac{i_B}{q}}{\frac{i_A}{p} + \frac{i_B}{q}} \tag{7.5}$$

where n_A and n_B are numbers of moles of components A and B. Hence, the current density ratio for the electrodeposition of these two metals should be defined as

$$\frac{i_A}{i_B} = \frac{p}{q}\frac{x}{(1-x)} \tag{7.6}$$

The condition defined by Eq. (7.6) could be achieved by proper adjustment of three essential variables: the concentration of the electrodepositing ions at the electrode/solution interface (where the discharge occurs), the electrode potential, and the temperature [1, 5].

For better understanding of the conditions defined by Eqs. (7.1, 7.2, 7.3, 7.4, 7.5, and 7.6), it is important to present polarization curves (current density vs. potential relationships) for electrodeposition of each metal. The characteristic cases are presented in Figs. 7.1 and 7.2. The first case is presented in Fig. 7.1a: the overpotential for electrodeposition of the more noble metal A is higher than that for the less noble metal B. From the potentials E_r(A) to E_r(B), only more noble metal electrodeposition occurs, while the electrodeposition of alloy commences at the potential E_1. In the potential range from E_r(B) to E_1, metal A electrodeposits with higher current density than metal B (the alloy contains more metal A than B). At the potential E_1, both metals electrodeposit with the same current density, and the alloy contains the same amount of both metals. At the potentials more negative than E_1, the metal B electrodeposits with higher current density and, accordingly, the alloy contains more metal B than metal A. The second case is presented in

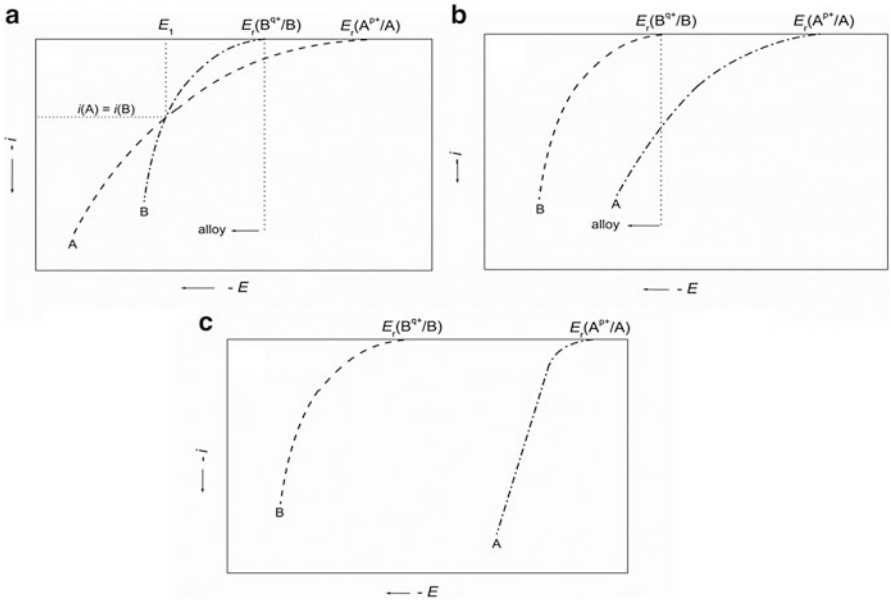

Fig. 7.1 Schematic presentation of the characteristic cases for alloy electrodeposition. (**a**) The overpotential for electrodeposition of the more noble metal A is higher than that for the less noble metal B; (**b**) The overpotential for electrodeposition of metal A is slightly lower than that for metal B; (**c**) Alloy electrodeposition is impossible (Reprinted from Ref. [5] with kind permission from Springer)

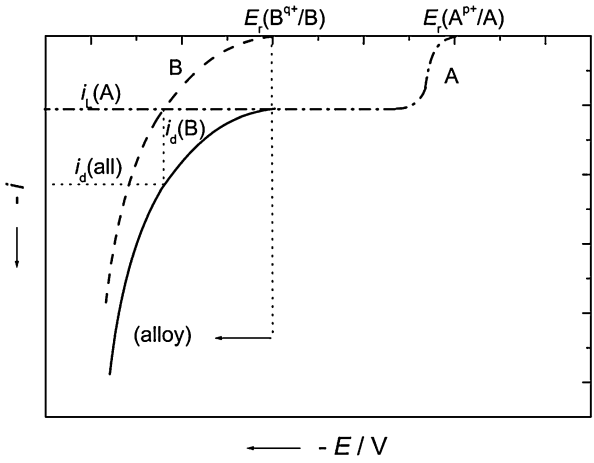

Fig. 7.2 Polarization curves for the electrodeposition of more noble metal (A) and less noble metal (B): $i_L(A)$ diffusion limiting current density for the electrodeposition of metal (A), $i_d(B)$ current density for the electrodeposition of metal (B), $i_d(all)$ current density for the electrodeposition of alloy (Reprinted from Ref. [5] with kind permission from Springer)

Fig. 7.1b: the overpotential for electrodeposition of metal A is slightly lower than that for metal B, i.e., the polarization curves are almost parallel. Hence, the electrodeposition of alloy commences at the potential E_r(B), while the alloy contains more metal A than B. If the difference between E_r(A) and E_r(B) is high and the overpotential for electrodeposition of the more noble metal A is lower than that for the less noble metal B, the third case presented in Fig. 7.1c applies: in such a case, alloy electrodeposition is impossible. The difference between the reversible potentials of two metals could be changed (lowered) by the change of metal ion concentration (activity), and in most cases, this is achieved by the complexation.

Simultaneous electrodeposition of two metals is possible even if the difference in their reversible potentials is high, if the applied current density for alloy electrodeposition is higher than the diffusion limiting current density for the electrodeposition of the more noble metal. Such a case is schematically presented in Fig. 7.2.

If $p = q = 2$, the molar ratios of metals (A) and (B) in the alloy are defined by the following relation:

$$x(\mathrm{A}) = \frac{i_\mathrm{L}(\mathrm{A})}{i_\mathrm{L}(\mathrm{A}) + i_\mathrm{d}(\mathrm{B})} = \frac{i_\mathrm{L}(\mathrm{A})}{i_\mathrm{d}(\mathrm{all})}$$
$$x(\mathrm{B}) = \frac{i_\mathrm{d}(\mathrm{B})}{i_\mathrm{L}(\mathrm{A}) + i_\mathrm{d}(\mathrm{B})} = \frac{i_\mathrm{d}(\mathrm{B})}{i_\mathrm{d}(\mathrm{all})} \tag{7.7}$$

7.2.2 *Types of Electrodeposition of Alloys*

Classification of different types of alloy electrodeposition was made by Brenner [3] in 1962, by defining five groups: equilibrium, irregular, regular, anomalous, and induced codeposition. More detailed explanations including samples for each type were given in Ref. [5].

7.2.2.1 Equilibrium Codeposition

Equilibrium codeposition implies a common reversible potential for both metal constituents so that the reduction of both metal ions would take place at potentials more negative than the reversible ones. To close the gap between the reversible potentials of electrodepositing metals, it is necessary to make the concentration of simple salts (undergoing complete dissociation) of the more noble metal impractically low and of the less noble metal impractically high. The best way to overcome this problem could result from complexation of metal ions with different ligands. Complexation usually changes the activity of the resulting species in solution by many orders of magnitude, while keeping the total amount of one or other metal in solution sufficiently high for a good supply of plating material to the cathode. It is very often case that the ions of both metals form complexes with one and the same

ligand with similar values of the stability (formation) constants, so that the change of the potential of the electrodeposition of each metal is the same (or similar) value. Usually, in such a case, the complexation with two different ligands could result in a more pronounced change of the electrodeposition potentials of two metals.

Electrodeposition of the Ni–Sn Alloy

In a further text, an example for the electrodeposition of Ni–Sn alloy from the solution containing pyrophosphate and glycine ligands is presented [6], where Sn belongs to the normal metals while Ni belongs to the inert metals (see Sect. 6.2). According to the literature [7], standard potential of the Ni electrodeposition is −0.23 V versus SHE, while that for Sn is −0.1364 V versus SHE and accordingly Ni is less noble metal. Taking into account that the overvoltage for Ni electrodeposition [8] is much higher than that for Sn electrodeposition [6], the difference between the potentials of electrodeposition of these two metals should be larger than that of their standard potentials. In the data presented in Dean's Handbook of Chemistry [9], Ni forms two pyrophosphate complexes, $[Ni(P_2O_7)]^{2-}$ and $[Ni(P_2O_7)_2]^{6-}$ as well as three glycine complexes, $[Ni(NH_2CH_2COO)]^{+}$, $[Ni(NH_2CH_2COO)_2]$, and $[Ni(NH_2CH_2COO)_3]^{-}$. All data about different complexes of Ni and Sn in the pyrophosphate and glycine solutions and corresponding reactions for their formation and their formation (stability) constants are given in the paper of Duffield et al. [10]. All species and their stability constants used for the calculation of the distribution of different complexes in the solution containing Sn, Ni, pyrophosphate, and glycine ions are listed in Table 7.1.

The calculation of the distribution of complexes in the solution containing pyrophosphate and glycine showed that $[Sn(P_2O_7)_2]^{6-}$ is dominant complex with Sn at pH 8.0, while two complexes of Ni dominate at a given pH: $[Ni(P_2O_7)_2]^{6-}$ and $[Ni(NH_2CH_2COO)_3]^{-}$. This is shown in Fig. 7.3.

The values of the equilibrium potentials (E_{eq}) of prevailing complexes, calculated using explanations based on the Gibbs energy change for reaction of certain complex formation [11] (assuming that the ions activities are equal to their concentrations), are also presented in Table 7.1. As can be seen, the equilibrium potential for electrodeposition of Sn by the reduction of $[Sn(P_2O_7)_2]^{6-}$ complex is −0.847 V versus SCE, while the equilibrium potentials for the reduction of $[Ni(P_2O_7)_2]^{6-}$ and $[Ni(NH_2CH_2COO)_3]^{-}$ complexes are more positive, being about −0.716 V versus SCE and situation becomes opposite to that for electrodeposition from the solution of simple ions. After the complexation Ni becomes more noble metal, while Sn becomes less noble one. Hence, it could be concluded that at pH 8.0 Sn would electrodeposit from the complex $[Sn(P_2O_7)_2]^{6-}$, while Ni would electrodeposit simultaneously from two complexes, $[Ni(P_2O_7)_2]^{6-}$ and $[Ni(NH_2CH_2COO)_3]^{-}$, in the presence of both complexing anions. The equilibrium potentials for electrodeposition of Sn and Ni still differ for 0.131 V. As already stated, because of high overpotential for Ni electrodeposition [6], it could be expected that two metals possess identical, or similar, potential of electrodeposition. This is exactly the case for these two metals in the pyrophosphate–glycine solution.

Table 7.1 All complexes present in the solution containing 0.1 M $SnCl_2 + 0.1$ M $NiCl_2 +$ 0.6 M $K_4P_2O_7 + 0.3$ M NH_2CH_2COOH, their concentrations, stability constants, and equilibrium potentials of prevailing complexes

Complexes	log β	Conc./M	E_{eq}/V vs. SCE
$[H(P_2O_7)]^{3-}$	8.14		
$[H_2(P_2O_7)]^{2-}$	14.01		
$[H_3(P_2O_7)]^{-}$	15.78		
$[H_4(P_2O_7)]$	16.63		
$[H(NH_2CH_2COO)]$	9.64		
$[H_2(NH_2CH_2COO)]^{+}$	12.05		
$[Sn\ (NH_2CH_2COO)H]^{2+}$	12.78		
$[Sn(NH_2CH_2COO)]^{+}$	10.02		
$[Sn(P_2O_7)]^{2-}$	13.05	0.007	−0.847
$[Sn(P_2O_7)H]^{-}$	15.92		
$[Sn(P_2O_7)H_2]$	17.47		
$[Sn(P_2O_7)_2]^{6-}$	16.27	0.093	−0.847
$[Sn(P_2O_7)_2H]^{5-}$	22.31		
$[Sn(P_2O_7)_2H_2]^{4-}$	26.79		
$[Sn(P_2O_7)_2H_3]^{3-}$	30.07		
$[Sn(P_2O_7)_2H_4]^{2-}$	31.58		
$[Sn(P_2O_7)OH]^{3-}$	5.32		
$[Sn(P_2O_7)(OH)_2]^{2-}$	−4.77		
$[Sn(P_2O_7)_2OH]^{5-}$	7.04		
$[Ni(NH_2CH_2COO)]^{+}$	5.60		
$[Ni(NH_2CH_2COO)_2]$	10.40	0.009	−0.716
$[Ni(NH_2CH_2COO)_3]^{-}$	13.80	0.057	−0.716
$[Ni(P_2O_7)]^{2-}$	5.80	0.005	−0.716
$[Ni(P_2O_7)_2]^{6-}$	7.40	0.029	−0.716

Reprinted from Ref. [5] with kind permission from Springer

The polarization curve for Ni–Sn alloy electrodeposition onto Ni electrode [12] is shown in Fig. 7.4. The electrodeposition process commences at about −0.83 V versus SCE being activation controlled down to about −0.95 V versus SCE, while in the potential range from about −0.95 V versus SCE to about −1.20 V versus SCE, well-defined diffusion limiting current density (−10 mA cm^{-2}) is established. In the region of the activation control (squares marked in Fig. 7.4a), Ni–Sn alloy coatings were electrodeposited at the current densities of −2, −4, and −6 mA cm^{-2}. Flat and compact electrodeposits of the thickness of about 5 μm were obtained in all cases, as shown in Fig. 7.4b. The composition of the coatings changed with the increase of cathodic current density from about 37 at.% Ni (for sample obtained at −2 mA cm^{-2}) to about 45 at.% Ni (for sample obtained at −6 mA cm^{-2}) [12], but in all cases, both metals were present in the coating, indicating a good example for equilibrium codeposition.

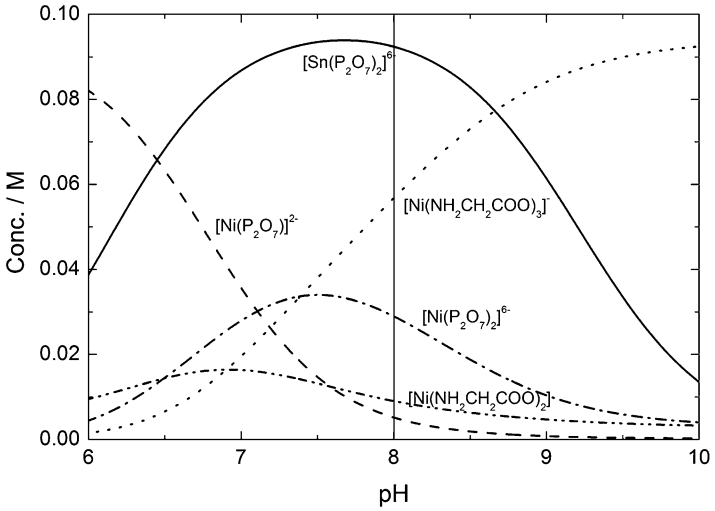

Fig. 7.3 Distribution of different complexes in the solution containing 0.1 M $SnCl_2 + 0.1$ M $NiCl_2 + 0.6$ M $K_4P_2O_7 + 0.3$ M NH_2CH_2COOH as a function of the solution pH (Reprinted from Ref. [5] with kind permission from Springer)

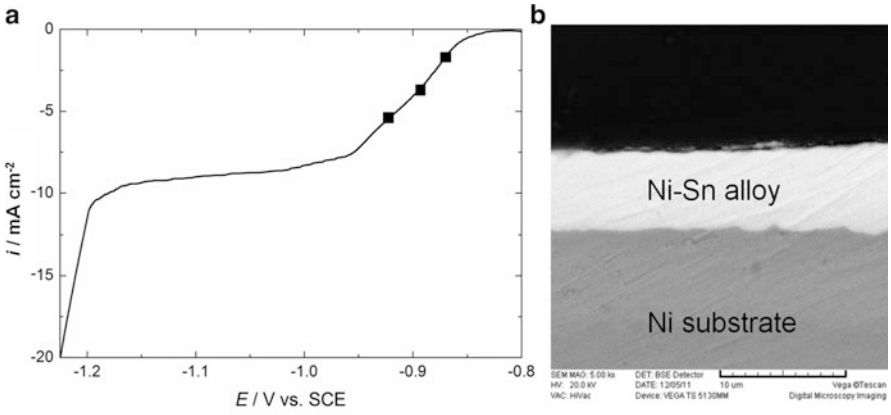

Fig. 7.4 (**a**) Polarization curve for electrodeposition of the Ni–Sn alloy onto Ni electrode. (**b**) Typical cross section of coatings obtained at different current densities marked in (**a**) with *solid squares* (■) (Reprinted from Ref. [5] with kind permission from Springer)

Morphology of the Ni–Sn Alloy

In this case, two electrodepositing metals are characterized by different mechanisms of electrodeposition: Sn nucleation is very fast with nuclei growing normal to the electrode surface, while nucleation of Ni is slow with lateral growth of the electrodeposit. In Fig. 7.5 are shown pure Sn electrodeposits obtained in two

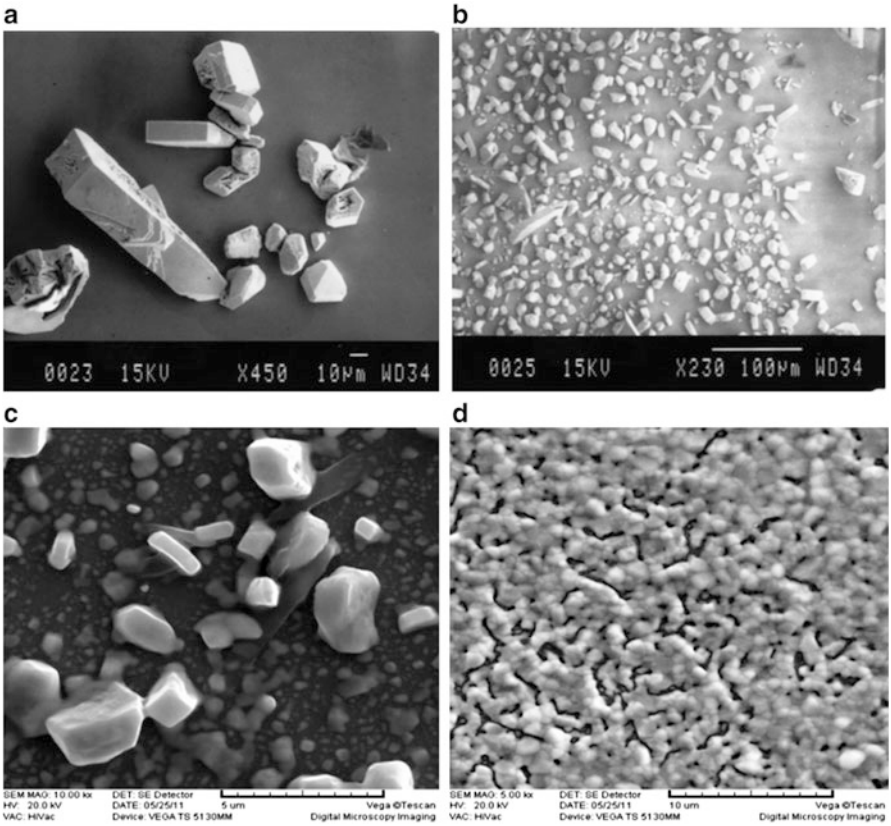

Fig. 7.5 SEM micrographs of the Sn electrodeposit obtained at the overpotentials of −20 mV (**a**) and −60 mV (**b**) on the 40 nm thick Cu layer evaporated onto Si(111) in the solution containing 0.5 M Sn–MSA + 1.0 M MSA. SEM micrographs of the Sn electrodeposit obtained onto Ni electrode during the potentiostatic pulse $E = -1.15$ V versus SCE for 1000 s in the solution 0.1 M $SnCl_2 + 0.6$ M $K_4P_2O_7 + 0.3$ M NH_2CH_2COOH of the pH 8.0, (**c**, **d**): (**c**) part of the surface with less dense electrodeposit; (**d**) part of the surface with more dense electrodeposit (Reprinted from Ref. [6] with the permission of The Electrochemical Society)

different solutions: SEM micrographs of the Sn electrodeposit obtained in the solution containing 0.5 M Sn–MSA + 1.0 M MSA (MSA – methane sulfonic acid) at the overpotentials of −20 mV (a) and −60 mV (b) on the 40 nm thick Cu layer evaporated onto Si(111); SEM micrographs of the Sn electrodeposit obtained onto Ni electrode during the potentiostatic pulse $E = -1.15$ V versus SCE for 1000 s in the solution 0.1 M $SnCl_2 + 0.6$ M $K_4P_2O_7 + 0.3$ M NH_2CH_2COOH of the pH 8.0, (c) and (d); (c) part of the surface with less dense electrodeposit; and (d) part of the surface with more dense electrodeposit [6]. Hence, under the conditions of constant potential (overpotential), it is practically not possible to obtain compact and flat Sn electrodeposit from the investigated solutions (without additives for brightening and leveling) independently of the materials and type of

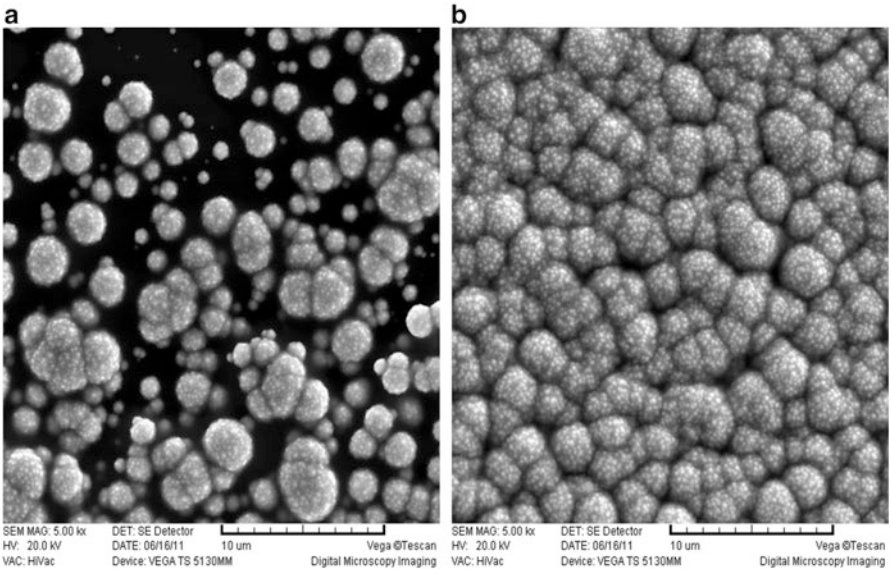

Fig. 7.6 SEM micrographs of the Ni–Sn electrodeposit obtained onto GC electrode during the potentiostatic pulse $E = -1.00$ V versus SCE for 1000 s in the solution 0.1 M $SnCl_2 + 0.1$ M $NiCl_2 + 0.6$ M $K_4P_2O_7 + 0.3$ M NH_2CH_2COOH of the pH 8.0: (**a**) less dense electrodeposit, average composition 54 at.% Ni–46 at.% Sn; (**b**) more dense electrodeposit, average composition 47 at.% Ni–53 at.% Sn

the electrode surface. Rectangular type crystals, growing normally to the electrode surface, are obtained in both cases.

During the initial period of Ni–Sn alloy electrodeposition, similar behavior could be detected with less and more dense parts of the electrodeposit, as shown in Fig. 7.6. In the case of alloy electrodeposition, the shape of crystals is different. Ball-like crystals with the average composition 54 at.% Ni–46 at.% Sn (the composition was obtained by the EDS analysis) could be detected at the less dense part of the electrodeposit (a), while the more dense part of the electrodeposit of the average composition 47 at.% Ni–53 at.% Sn is characterized with distorted balls (b). After prolonged electrodeposition in the range of activation-controlled electrodeposition ($i \leq 10$ mA cm^{-2}, Fig. 7.4a), compact electrodeposit is obtained [6], as shown in Fig. 7.4b.

At higher cathodic current densities (potentials more negative than -1.2 V versus SCE, Fig. 7.4a), sudden increase of current density indicates simultaneous evolution of hydrogen. In such a case, the morphology of electrodeposited Ni–Sn alloy coatings [12] changes from the flat into nodular one, with the appearance of large, micron-sized pores, as shown in Fig. 7.7 for the Ni–Sn electrodeposit obtained at the current density of -75 mA cm^{-2}.

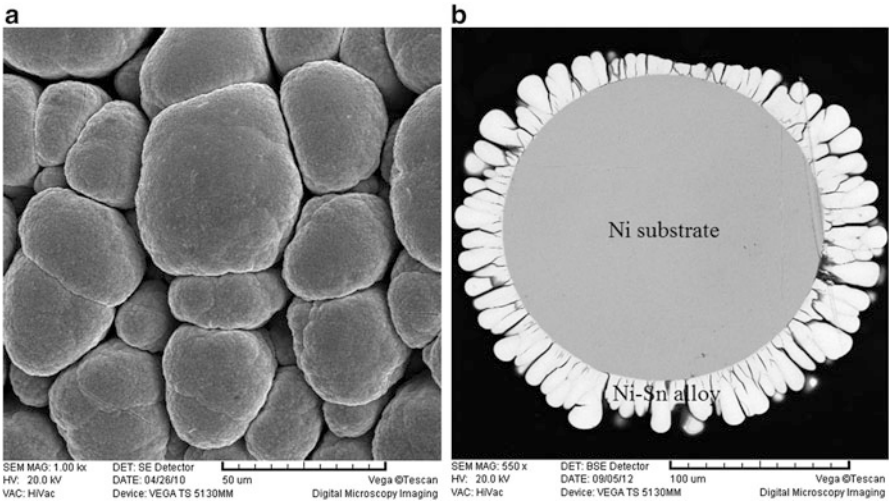

Fig. 7.7 SEM micrographs of the Ni–Sn electrodeposit obtained onto Ni 40 mesh electrode at $i = -75$ mA cm^{-2} in the solution 0.1 M $SnCl_2 + 0.1$ M $NiCl_2 + 0.6$ M $K_4P_2O_7 + 0.3$ M NH_2CH_2COOH of the pH 8.0: (**a**) surface of the electrodeposit; (**b**) cross section of the electrodeposit

7.2.2.2 Irregular Codeposition

The irregular type of codeposition is very often characterized by simultaneous influence of cathodic potential and diffusion phenomena, i.e., it mainly occurs under the activation and/or mixed control of the electrodeposition processes. The rate of electrodeposition in such a case is expressed by the Butler–Volmer equation which is usually used for the kinetics of electrochemical processes [1, 5]:

$$\frac{i}{i^{\mathrm{o}}} = \frac{i_{\mathrm{o}}}{i^{\mathrm{o}}}\left[\exp\left(\frac{\alpha_a F}{RT}\eta\right) - \left(\frac{c}{c_{\mathrm{o}}}\right)\exp\left(\frac{-\alpha_c F}{RT}\eta\right)\right] \tag{7.8}$$

where $\eta = E - E_{\mathrm{r}}$ corresponds to the overpotential needed for the electrodeposition of metals (see Eq. (7.1)), c and c_{o} represent concentrations of the discharging species at the surface of the electrode and in the bulk of the solution, respectively, i_{o} is "exchange current density" related to the rate constant of the electrodeposition process, and α_{a} and α_{c} are anodic and cathodic transfer coefficients related to the mechanism of discharge (note that for a cathodic process, both η and i acquire negative signs. Also note that the current densities are divided by arbitrarily chosen unit current i^{o} in order to obtain dimensionless values for further use).

If the discharge of electrodepositing species is sufficiently slow so that their supply to the electrode surface occurs without difficulty, the concentration c virtually does not deviate from c_{o}, and such a case is termed "activation-controlled" electrodeposition with the rate-determining step being the activation energy of the discharge process. At any cathodic overpotential larger than −40 mV,

the first term in Eq. (7.8) becomes negligible, so that this equation can be transformed into a simpler one, known as the Tafel equation:

$$\eta = a - b\log\left(-\frac{i}{i^{o}}\right) \tag{7.9}$$

where the Tafel constant a is

$$a = \frac{2.3RT}{\alpha_c F}\log\left(\frac{i_o}{i^{o}}\right) \tag{7.10}$$

while the slope of the linear dependence obtained from a plot η versus $\log(-i)$ (Tafel slope) is

$$b = \frac{2.3RT}{\alpha_c F} \tag{7.11}$$

The above reasoning applies equally and independently to both metals (A) and (B), i_A and i_B, and the total current density being $i_{alloy} = i_A + i_B$.

It should be stated here that the concept of overpotential is related to the reversible potential of a pure metal in a given solution. In the case of codeposition of two metals and the formation of a phase $A_xB_{(1-x)}$, this potential has no physical meaning since it represents an arbitrary point to which i_o is related.

Electrodeposition of the Ag–Cd Alloy

An example for irregular codeposition is presented in Fig. 7.8 for the system Ag–Cd (two intermediate metals). The Ag, Cd, and Ag–Cd alloy coatings were electrodeposited onto stationary Pt electrode from cyanide electrolytes [13], using the following solutions respectively: 0.14 M $CdSO_4{\cdot}8/3H_2O + 0.56$ M KCN, 0.032 M $KAg(CN)_2 + 0.56$ M KCN, and 0.032 M $KAg(CN)_2 + 0.14$ M $CdSO_4{\cdot}8/3H_2O + 0.56$ M KCN. Figure 7.8 shows polarization curves recorded at a sweep rate of 1 mV s^{-1} in the electrolyte containing both metals separately or together. The electrodeposition of Ag (dashed line) is characterized by the cathodic shoulder, which is most likely indication of the diffusion limiting current density (taking into account small concentration of Ag) at a potential of about −0.82 V versus Ag/AgCl, with the electrodeposition starting at about −0.79 V versus Ag/AgCl. The increase of the cathodic current density at potentials more negative than −1.2 V versus Ag/AgCl during the Ag electrodeposition is the consequence of simultaneous hydrogen evolution. Pure Cd electrodeposition (dotted line) starts at the same potential as that of Ag. At potentials more negative than −1.6 V versus Ag/AgCl current oscillations with amplitude higher than 10 mA cm^{-2} have been observed. In the case of Ag–Cd alloy electrodeposition, a shoulder representing diffusion-controlled electrodeposition of Ag (solid line) appears at about −0.51 V versus Ag/AgCl (for about 0.3 V

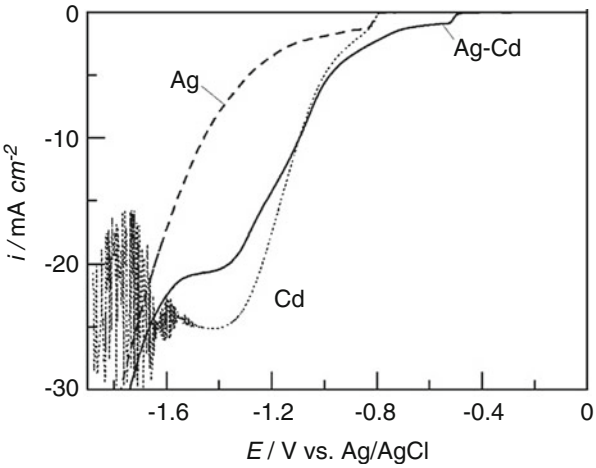

Fig. 7.8 Polarization curves recorded at a sweep rate of 1 mV s^{-1} in the electrolyte containing 0.032 M $KAg(CN)_2 + 0.56$ M KCN (Ag), 0.14 M $CdSO_4 \cdot 8/3H_2O + 0.56$ M KCN (Cd), and 0.032 M $KAg(CN)_2 + 0.14$ M $CdSO_4 \cdot 8/3H_2O + 0.56$ M KCN (Ag–Cd) (Reprinted from Ref. [5] with kind permission from Springer)

Table 7.2 Concentration of different Ag complexes and their equilibrium potentials (E_{eq})

Solution composition	Concentration / %		E_{eq}/V versus Ag/AgCl		
	$[Ag(CN)_2]^-$	$[Ag(CN)_3]^{2-}$	$[Ag(CN)_4]^{3-}$	$[Ag(CN)_3]^{2-}$	$[Ag(CN)_2]^-$
Pure Ag electrodeposition	35.9	61.2	2.6	−0.737	
Ag–Cd alloy electrodeposition	98.1	1.9	–		−0.479

Reprinted from Ref. [5] with kind permission from Springer

more positive than the shoulder of pure Ag). Hence, in the solution containing both metal ions, electrodeposition of Ag commences at more positive potential. In order to find out the reason for such behavior, the analysis of Ag complexes with cyanide has been performed. The results are presented in Table 7.2. As can be seen, when pure Ag is present in the KCN solution the dominant complex is $[Ag(CN)_3]^{2-}$, with the equilibrium potential of −0.737 V versus Ag/AgCl. In the presence of Cd ions, most of the CN^- anions are consumed in Cd–CN complexes ($[Cd(CN)]^+$, $[Cd(CN)_2]$, $[Cd(CN)_3]-$, and $[Cd(CN)_4]^{2-}$) and the dominant Ag–CN complex becomes $[Ag(CN)_2]^-$, with the equilibrium potential of −0.479 V versus Ag/AgCl. Hence, from the presented analysis, it is obvious that the first shoulder on a solid curve in Fig. 7.8 for Ag–Cd alloy electrodeposition corresponds to the electrodeposition of pure Ag from $[Ag(CN)_2]^-$ complex [13, 14].

Morphology of the Ag–Cd Alloy

Five alloy samples were electrodeposited to the total charge of -1.3 C cm^{-2} at different potentials (-1.0, -1.4, -1.6, -1.8, and -2.0 V versus Ag/AgCl). The morphology of the coating electrodeposited at -1.0 V versus Ag/AgCl is presented in Fig. 7.9. The morphology of this coating is typical to those where the gradual increase in crystallite size with increase in Cd content is observed [13, 14]. At more negative potential (-1.4 V versus Ag/AgCl), the coating becomes very heterogeneous (see Fig. 7.10a) and reflections of Cd, $AgCd_3$, AgCd, and Ag phases were registered on the XRD spectra [13]. The heterogeneity of the coating could be the consequence of two factors: the alloy composition and the influence of simultaneous hydrogen evolution, since the natural convection must be significantly disturbed by the hydrogen evolution at this potential.

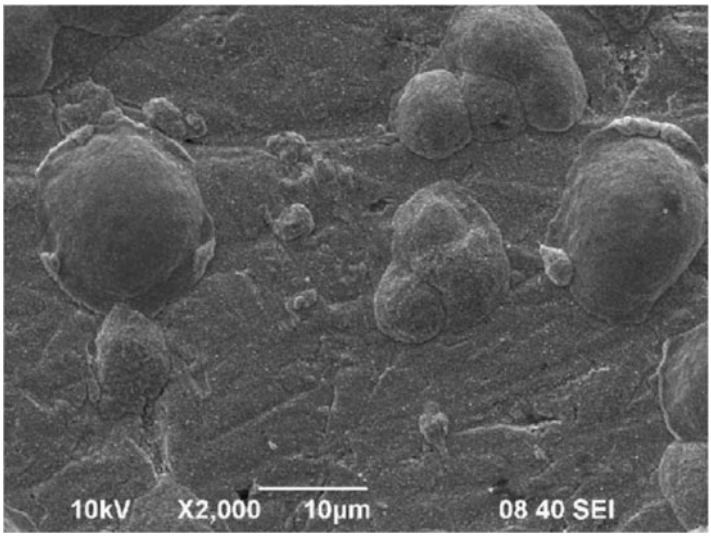

Fig. 7.9 Surface morphology (SEM) of the alloy coating electrodeposited at a potential $E = -1.0$ V versus Ag/AgCl (Reprinted from Ref. [13] with permission from Elsevier)

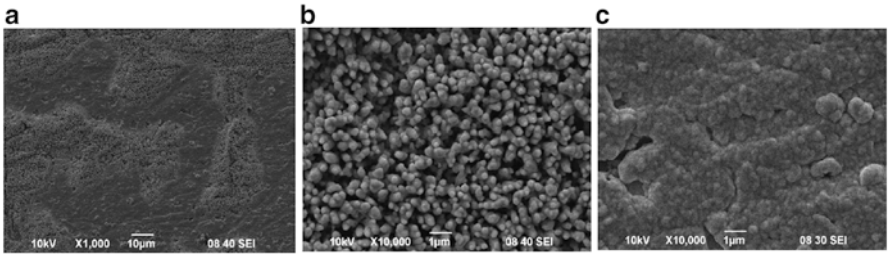

Fig. 7.10 (**a**) Surface morphology (SEM) of the alloy coating electrodeposited at $E = -1.4$ V versus Ag/AgCl. (**b**, **c**) different areas of the same coating at higher magnification (Reprinted from Ref. [13] with permission from Elsevier)

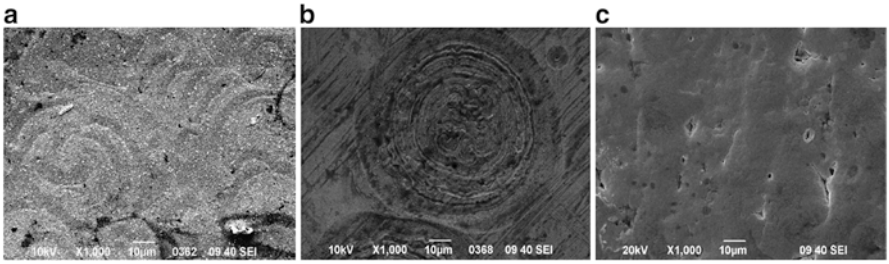

Fig. 7.11 Surface morphology (SEM) of alloy coatings electrodeposited at different (more negative) potentials: (**a**) $E = -1.6$ V versus Ag/AgCl; (**b**) $E = -1.8$ V versus Ag/AgCl; (**c**) $E = -2.0$ V versus Ag/AgCl (Reprinted from Ref. [13] with permission from Elsevier)

The heterogeneity of this coating is well visible – its morphology is presented in Fig. 7.10a. In the rough areas of the coating, the Cd content is about 40 at.% (Fig. 7.10b), while in the smooth areas, it reaches 58 at.% (Fig. 7.10c). The electrodeposition at higher cathodic potentials, −1.6 or −1.8 V versus Ag/AgCl, leads to the appearance of some periodic structured areas on the surface (Fig. 7.11a, b, special structures observed in alloy electrodeposits only; see Sect. 7.2.3), and the reflections of pure Cd disappear on the XRD, which could be connected with the changes in the current efficiency and the enhanced formation of Ag–Cd alloy phases. At the most negative potential of −2.0 V versus Ag/AgCl, the phase $AgCd_3$ is preferentially formed and mainly the reflections corresponding to this phase are registered on the XRD spectra. The morphology of this coating is shown in Fig. 7.11c. The surface is smooth and shiny, indicating the presence of mainly one phase in the electrodeposit ($AgCd_3$) [13].

7.2.2.3 Regular Codeposition

Regular codeposition assumes transport-controlled codeposition in which diffusion of metal ions of both metals is a rate-determining step in the overall codeposition reaction [1, 5].

Under steady-state conditions of electrodeposition, the diffusion is governed by Fick's first law [15].

$$\frac{c}{c_o} = \frac{i_L + i}{i_L} \tag{7.12}$$

with

$$i_L = \frac{zFD}{\delta} c_o \tag{7.13}$$

where D is the diffusion coefficient of the electrodepositing species and δ is the Nernst diffusion layer thickness.

Introducing Eq. (7.12) into Eq. (7.8) and rearranging following relation is obtained:

$$i = \frac{i_o\left[\exp\left(\frac{\alpha_a F}{RT}\eta\right) - \exp\left(-\frac{\alpha_c F}{RT}\eta\right)\right]}{1 + \frac{i_o}{i_L}\exp\left(-\frac{\alpha_c F}{RT}\eta\right)} \tag{7.14}$$

At increasing values of overpotential, the second term in the denominator becomes overwhelming and the current density tends to a potential-independent diffusion limiting one, i_L.

Under the conditions of diffusion control, a plot of E versus log $[(-i_L/i)-1]$ should be made instead of the regular Tafel plot and the relationship should be linear with the slope of $(2.3RT/\alpha_c F)$.

Electrodeposition of the Ag–Pd Alloy

One of the examples of regular codeposition is the electrodeposition of Ag–Pd alloy from high concentration chloride (12 M LiCl) containing bath [16] (both metals belong to intermediate metals due to complexation with Cl^- ions). Polarization curves for the electrodeposition of Ag–Pd alloy from the solution containing 0.005 M $PdCl_2$ + 0.05 M AgCl + 12 M LiCl + 0.1 M HCl ($t = 80$ °C), recorded onto rotating glassy carbon electrode under the conditions of stationary (RPM = 0)

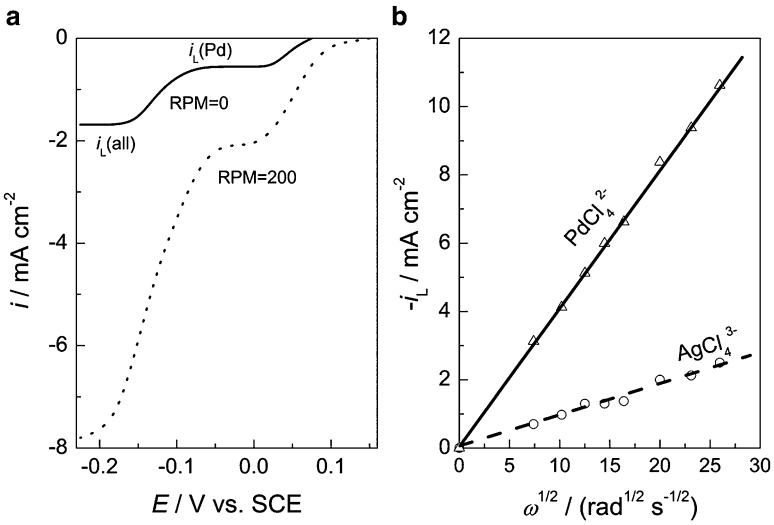

Fig. 7.12 (**a**) Polarization curves for the electrodeposition of Ag–Pd alloy from the solution containing 0.005 M $PdCl_2$ + 0.05 M AgCl + 12 M LiCl + 0.1 M HCl ($t = 80$ °C), recorded onto rotating glassy carbon electrode. (**b**) The i_L versus $\omega^{1/2}$ dependences for pure Ag and pure Pd electrodeposition onto rotating glassy carbon electrode from the solution containing 0.005 M $PdCl_2$ + 12 M LiCl + 0.1 M HCl and 0.005 M AgCl + 12 M LiCl + 0.1 M HCl, respectively ($t = 80$ °C) (Reprinted from Ref. [5] with kind permission from Springer)

and convective (RPM = 200) diffusion, are presented in Fig. 7.12a. The Pd electrodeposition commences at about 0.07 V versus SCE, while the codeposition of Ag begins at about −0.07 V versus SCE. A well-defined diffusion limiting current densities for Pd (i_L(Pd)) and alloy (i_L(alloy)) electrodeposition, representing actually the sum of i_L(Pd) and i_L(Ag), could be detected on the polarization curves, indicating that the i_L(Ag) is lower than that of Pd (taking into account that the concentration of AgCl is ten times higher than that of $PdCl_2$) and that the diffusion coefficient for Ag electrodeposition is lower than that for Pd. This is confirmed in Fig. 7.12b. The electrodeposition of Pd occurs by the reduction of $[PdCl_4]^{2-}$, while the electrodeposition of Ag occurs by the reduction of $[AgCl_4]^{3-}$.

The linear i_L versus $\omega^{1/2}$ dependences [16] (Fig. 7.12b) confirm that the diffusion of both species obeys Levich's Eq. (7.15) and from their slopes the diffusion coefficients are obtained. Corresponding values of D for both species amounts to $D([AgCl_4]^{3-}) = 5.5 \times 10^{-6}$ cm^2·s^{-1} and $D([PdCl_4]^{2-}) = 1.8 \times 10^{-5}$ cm^2·s^{-1}:

$$i_L = 0.62zFD^{2/3}\nu^{-1/6}c_o\omega^{1/2} \tag{7.15}$$

(ν – kinematic viscosity, ω – rotation speed).

In the case of Ag–Pd electrodeposition from ammoniacal electrolyte, the same type of electrodeposition (regular) is valid, but the potentials of electrodeposition of individual metals are opposite [17] to those in chloride-containing electrolyte: Ag is more noble metal with its electrodeposition commencing at about −0.05 V versus Ag/AgCl being characterized by well-defined diffusion limiting current density of about −0.95 mA cm^{-2}, while Pd is less noble metal starting to electrodeposit at about −0.40 V versus Ag/AgCl, as shown in Fig. 7.13. Such behavior is the result of

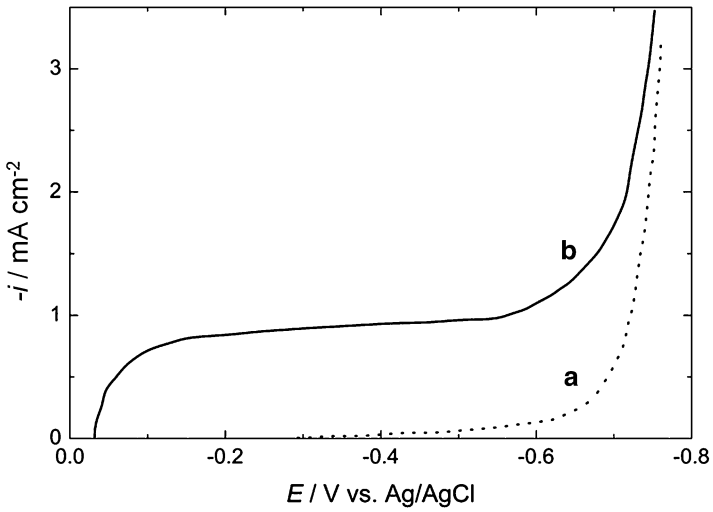

Fig. 7.13 Polarization curves for Pd and Ag–Pd electrolytes ($v = 1$ mV s^{-1}): (**a**) 20 g dm^{-3} Pd; (**b**) 2 g dm^{-3} Ag + 20 g dm^{-3} Pd; pH 11.5 adjusted by addition of NH_3 (Reprinted from Ref. [17] with the permission of Johnson Matthey Plc)

much stronger complexation of Pd^{2+} with NH_3 causing more negative potential for Pd electrodeposition (stability constant for complex $[Pd(NH_3)_4]^{2+}$ amounts to 6.3×10^{32}, while that for $[Ag(NH_3)_2]^{+}$ amounts to 1.6×10^{7}).

Morphology of the Ag–Pd Alloy

Morphology of Ag–Pd alloys electrodeposited from the ammonium-containing electrolyte [17] is shown in Fig. 7.14. At small current density, (a) matt electrodeposit was obtained, while at high current density, (b) bright electrodeposit was obtained, due to decrease of Ag content in the alloy.

Morphology of the Ag–Pd alloy of approximate composition 50 at.% Ag – 50 at. % Pd obtained from the chloride-containing electrolyte [16] is similar to that presented in Fig. 7.14 for $i = -$ 15 mA cm^{-2} (semi-bright).

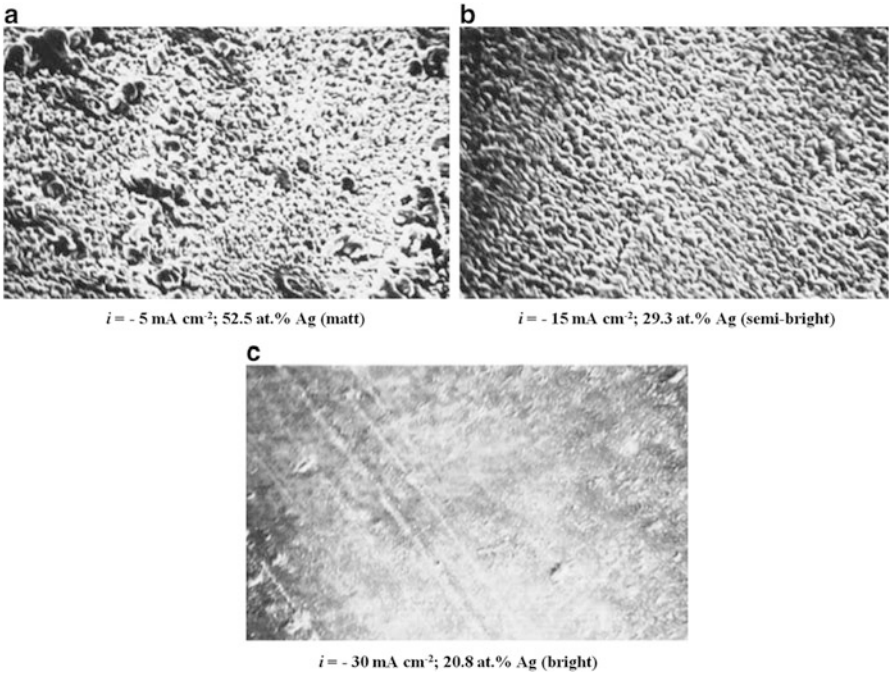

Fig. 7.14 SEMs of the surface of Ag–Pd alloys electrodeposited at different current densities from the ammoniacal solution containing 3 g dm^{-3} Ag + 20 g dm^{-3} Pd (Reprinted from Ref. [17] with the permission of Johnson Matthey Plc)

Electrodeposition of the Ag–Sn Alloy

Two types of solutions were examined for Ag–Sn alloy electrodeposition [18]: sulfate solution containing thiourea as a complexing agent for Ag^+ ions and pyrophosphate and iodide solution which form a stable complex with both Ag^+ and Sn^{2+} ions. In sulfate solution, Sn was a normal metal, while Ag was intermediate one due to formation of complexes with thiourea and iodide ions. In pyrophosphate solution, both metals belonged to intermediate ones due to formation of complexes with pyrophosphate and iodide ions. The polarization curves for alloy electrodeposition measured by the potential sweep method ($v = 0.5$ mV s^{-1}) in sulfate and pyrophosphate–iodide solutions are shown in Fig. 7.15. A current density rapidly increased at about −0.07 V versus NHE with the current density plateau up to about −0.27 V versus NHE corresponding to the pure Ag electrodeposition in the sulfate solution. Additional current density increase and plateau at more negative potentials correspond to the alloy electrodeposition (①). Similar behavior is detected for pyrophosphate–iodide solution (②). In both electrolytes, electrodeposition of both metals was suppressed due to complexes formation. The content of Ag in both cases abruptly decreased with the increase of electrodeposition current density.

Morphology of the Ag–Sn Alloy

Morphology of Ag–Sn alloy electrodeposits obtained from sulfate solution at different current densities is presented in Fig. 7.16, while the morphology of the same alloy electrodeposits obtained from pyrophosphate–iodide solution at different current densities is presented in Fig. 7.17.

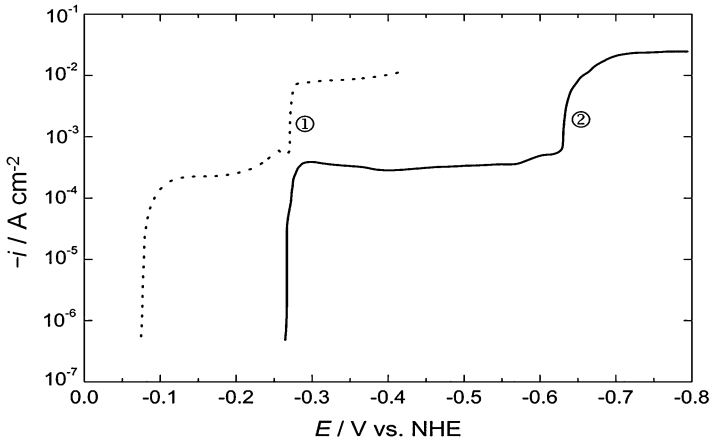

Fig. 7.15 Polarization curves for Ag–Sn alloy electrodeposition from sulfate (①) and pyrophosphate–iodide (②) solutions (Reprinted from Ref. [18] with the permission of the Japan Institute of Metals and Materials)

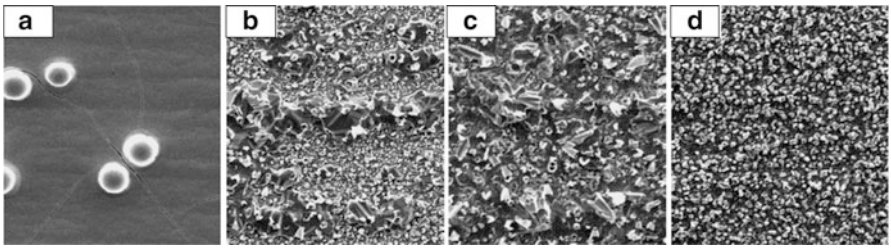

Fig. 7.16 Morphology of Ag–Sn electrodeposits obtained from sulfate solution at different current densities. (**a**) $i = -0.2$ mA cm^{-2}, 98 mass % Ag; (**b**) $i = -1.0$ mA cm^{-2}, 45 mass % Ag; (**c**) $i = -2.0$ mA cm^{-2}, 20 mass % Ag; (**d**) $i = -10.0$ mA cm^{-2}, 13 mass % Ag (Reprinted from Ref. [26] with the permission of Journal of Chemical Sciences)

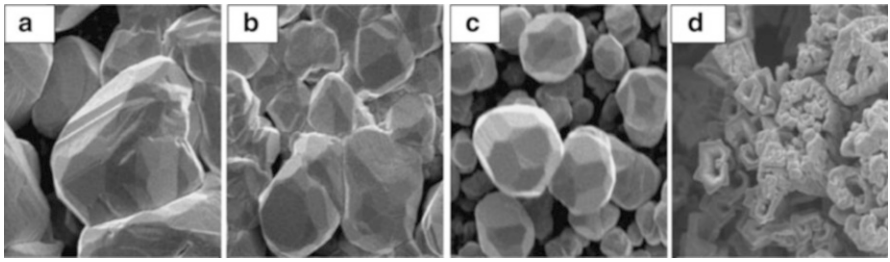

Fig. 7.17 Morphology of Ag–Sn electrodeposits obtained from pyrophosphate–iodide solution at different current densities. (**a**) $i = -0.2$ mA cm^{-2}, 100 mass % Ag; (**b**) $i = -0.4$ mA cm^{-2}, 81 mass % Ag; (**c**) $i = -0.5$ mA cm^{-2}, 77 mass % Ag; (**d**) $i = -0.6$ mA cm^{-2}, 62 mass % Ag (Reprinted from Ref. [26] with the permission of Journal of Chemical Sciences)

At a current density of -0.2 mA cm^{-2} (a), Fig. 7.16, the electrodeposit of practically pure Ag (98 mass % Ag) showed a smooth surface despite partial grains and cracks in the smooth area. At a current density of -1.0 mA cm^{-2} (b), the content of Ag decreased to 45 mass %, the smooth area disappeared, and the electrodeposit consisted of grains over the entire surface. Further increase in the cathodic current density to -2.0 mA cm^{-2} (c) and -10.0 mA cm^{-2} (d) caused smaller grains and significant decrease of the Ag content.

The surface morphology of Ag–Sn alloys electrodeposited from a pyrophosphate–iodide solution was completely different. At the smallest electrodeposition current density ($i = -0.2$ mA cm^{-2}), it consisted of large blocks, while at $i = -0.6$ mA cm^{-2}, the electrodeposit became coarse and spongy (Fig. 7.17) [18].

7.2.2.4 Anomalous Codeposition

According to Brenner's classification [3], anomalous codeposition is characterized by the fact that the less noble metal electrodeposits before the more noble one as the potential is driven cathodic. As a consequence, the content of the less noble metal in

the alloy is higher than its content in the solution. In all cases of anomalous codeposition, both metals belong to the group of intermediate metals [1, 5].

Electrodeposition of the Co–Ni Alloy

An excellent example [19] is found in the case of Co–Ni alloy electrodeposition, where both metals belong to the inert metals. Pure Co and pure Ni were electrodeposited at RPM = 1000 onto a gold disc electrode from the solutions containing 0.2 M $CoSO_4 + 0.2$ M $Na_3C_6H_5O_7$ and 1 M $NiSO_4 + 0.2$ M $Na_3C_6H_5O_7$ respectively. For electrodeposition of their alloys of different compositions, only the concentration of Co^{2+} has been changed, being 0.005 M, 0.01 M, 0.025 M, 0.05 M, and 0.2 M, respectively. Alloy layers of different compositions of the thickness of approximately 0.34 μm were obtained by galvanostatic electrodeposition at two different current densities ($i = -2.5$ mA cm^{-2} (○) and $i = -28.5$ mA cm^{-2} (□)) to the same amount of charge ($Q_{dep} = -1$ C cm^{-2}). Polarization curves for pure metal electrodeposition (Co and Ni) and Co–Ni alloy electrodeposition (alloy) from the solution containing 0.025 M $CoSO_4 + 1$ M $NiSO_4 + 0.2$ M $Na_3C_6H_5O_7$ are presented in Fig. 7.18a (all other polarization curves for Co–Ni alloy electrodeposition are placed between that for Ni and that for alloy – shaded area). As can be seen, all polarization curves for Co–Ni alloy electrodeposition are placed at more positive potentials than either of pure metals, which is clear indication for the anomalous codeposition of these two metals.

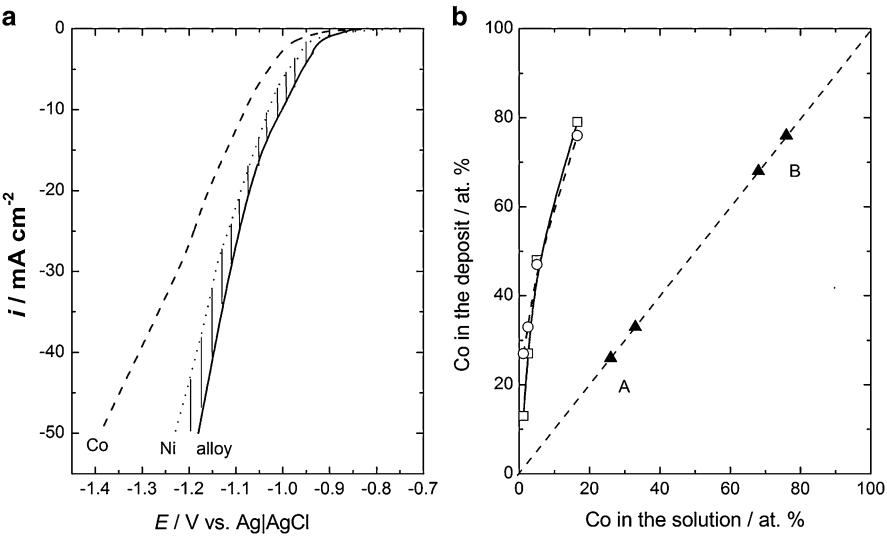

Fig. 7.18 (**a**) Polarization curves (corrected for IR drop) for the electrodeposition of pure metals (Co and Ni) and Co–Ni alloy at the gold disc electrode (RPM = 1000) obtained from the solutions: 0.2 M $CoSO_4 + 0.2$ M $Na_3C_6H_5O_7$ (Co); 1 M $NiSO_4 + 0.2$ M $Na_3C_6H_5O_7$ (Ni); 0.025 M $CoSO_4 +$ 1 M $NiSO_4 + 0.2$ M $Na_3C_6H_5O_7$ (alloy). (**b**) Brenner's diagram for the system Co–Ni: samples electrodeposited at $i = -2.5$ mA cm^{-2} (○) and at $i = -28.5$ mA cm^{-2} (□) (Reprinted from Ref. [5] with kind permission from Springer)

Based on the chemical analysis, the content of Co in the electrodeposit increases within the range ~8 at. % to ~80 at. % with increasing concentration of Co^{2+} ions in the solution. Brenner's diagram presented in Fig. 7.18b clearly shows pronounced anomalous codeposition.

Different explanations for such behavior are offered in the literature [3]. The most likely one appears to be "the hydroxide suppression mechanism" [20– 23]. According to this concept, coevolution of hydrogen during the electrodeposition causes an increase of pH at the electrode/solution interface, producing hydrolysis of less noble metal species and their precipitation as a layer of solid hydroxide. Formed hydroxide layer provides a good supply of ions of the less noble metal for their discharge and electrodeposition but suppresses the transport of species of the more noble metal to the cathode surface, causing anomalous codeposition.

Morphology of the Co–Ni Alloy

Co–Ni alloys were electrodeposited from a typical Watts-type electrolyte, containing $NiSO_4$ (200 g dm^{-3}), NaCl (20 g dm^{-3}), H_3BO_3 (30 g dm^{-3}), sodium lauryl sulfate (0.1 g dm^{-3}), and $CoSO_4$ (0–80 g dm^{-3}) [24]. Alloys were electrodeposited on AISI-1045 steel substrates at a current density of −30 mA cm^{-2}, bath temperature of 45 °C, and pH 4.0. The dependence of the morphology on the composition is shown in Fig. 7.19.

Typical morphology of a Watts Ni electrodeposit is shown in Fig. 7.19a, characterized with relatively large grain size (3–10 μm) and polyhedral crystallites. With the increase of Co content from 7 to 49 wt. % (Fig. 7.19b–d), a gradual decrease in the grain size of the Co–Ni alloy down to a submicron grain size is observed. When the Co content reached the 49 wt. %, close observation of SEM morphology at high magnification (Fig. 7.19g) revealed that the Co–Ni alloys have spherical cluster surface piled with a large number of equally sized grains with

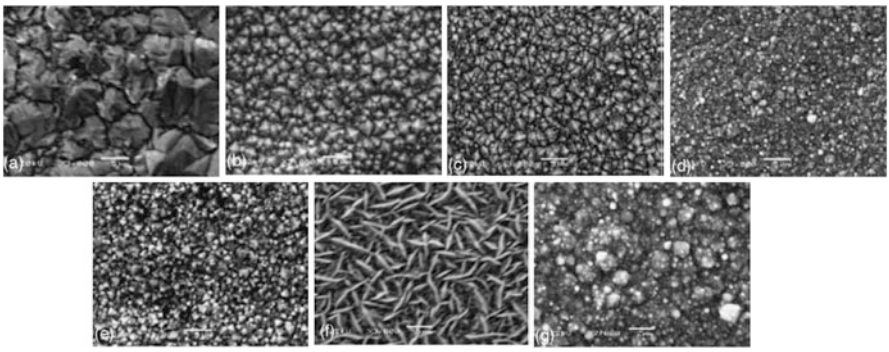

Fig. 7.19 SEM morphologies of Co–Ni alloy electrodeposits with their Co contents of (**a**) 0 wt.%, (**b**) 7 wt.%, (**c**) 27 wt.%, (**d**) 49 wt.%, (**e**) 66 wt.%, (**f**) 81 wt.%, (**g**) high magnification of Ni–49 wt.% Co alloy (Reprinted from Ref. [24] with the permission of Elsevier)

spherical shape. At above 49 wt. % Co, the grain size of Co–Ni electrodeposits, however, increased with the increase of Co content in alloys. When increasing Co content up to 81 wt. %, the morphology of the Co–Ni alloys changed dramatically, and with less compact structure, the Co–Ni alloy showed a rather regularly branched structure with extended acicular 3–6 μm length crystallites (Fig. 7.19f). Such a change of the morphology is related to the change in the phase composition of electrodeposited Co–Ni alloys. XRD investigations revealed that the phase structure of Co–Ni alloys gradually changed from *fcc* into *hcp* with the increase of Co content [24].

The influence of saccharin addition on the morphology and nanostructure of Co–Ni electrodeposits containing 80 at.%·Co was investigated by SEM and TEM analysis [25]. Alloys were electrodeposited from the bath containing 30 g dm^{-3} $NiSO_4 \times 6H_2O$, 30 g dm^{-3} $CoSO_4 \times 7H_2O$, 15 g dm^{-3} $NiCl_2 \times 6H_2O$, 15 g dm^{-3} H_3BO_3, and 10 g dm^{-3} NaCl at $i = -5.1$ mA cm^{-2}, while the amount of added saccharin varied from 0 to 12 g dm^{-3}. Figure 7.20 shows that already at 2 g dm^{-3} flat and nanocrystalline electrodeposit was obtained. The grain size of these electrodeposits sharply decreased from 50 to 5 nm with the increase of the amount of added saccharin from 0.0 to 0.05 g dm^{-3}, while slight increase of the grain size to about 10 nm at saccharin concentrations higher than 1 g dm^{-3} was detected by XRD.

TEM analysis of the electrodeposit with the lowest grain size of 5 nm (amount of saccharin 0.05 g dm^{-3}) is shown in Fig. 7.21a, while that of the electrodeposit obtained at saccharin concentration of 2.0 g dm^{-3} is shown in Fig. 7.22b. Dark-field image (Fig. 7.21a) shows grains of 30 nm size, containing a high density of nanoscale twins. In the electrodeposit obtained from the bath containing 2.0 g dm^{-3} of saccharin [25] (Fig. 7.21b), nanocrystalline grains are smaller (about 20 nm). Nanoscale twins are also present, although the twin density is somewhat lower than that observed in Fig. 7.21a.

Electrodeposition of the Fe–Zn Alloy

In this case, alloy contains normal (Zn) and inert (Fe) metal. Electrodeposition of Fe–Zn alloy was carried out from the sulfate bath [26]. The optimized composition

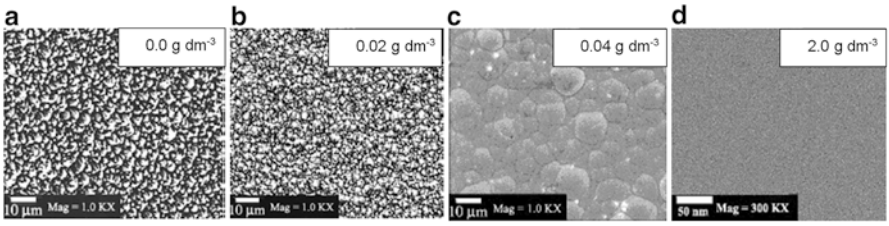

Fig. 7.20 The effect of saccharin addition on the topography of electrodeposited Co 80 at.% -Ni 20 at.% *hcp* alloys. (**a**) 0.0 g dm^{-3} saccharin; (**b**) 0.02 g dm^{-3} saccharin; (**c**) 0.04 g dm^{-3} saccharin; (**d**) 2.0 g dm^{-3} saccharin (Reprinted from Ref. [25] with kind permission from Springer)

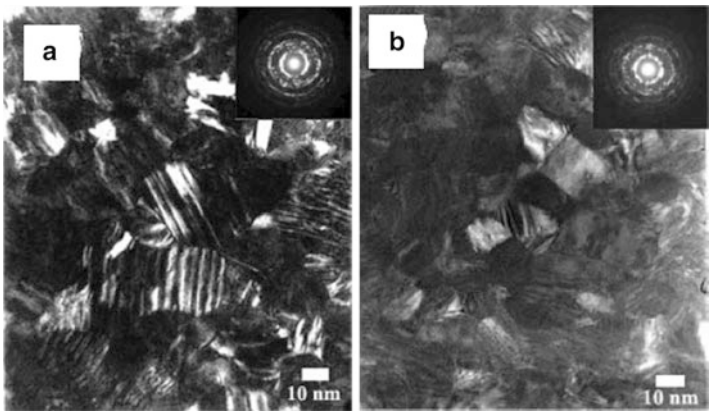

Fig. 7.21 Dark-field TEM images of the Co–Ni electrodeposits containing 80 at. % Co, electrodeposited with 0.05 g dm^{-3} (**a**) and 2.0 g dm^{-3} (**b**) of saccharine (Reprinted from Ref. [25] with kind permission from Springer)

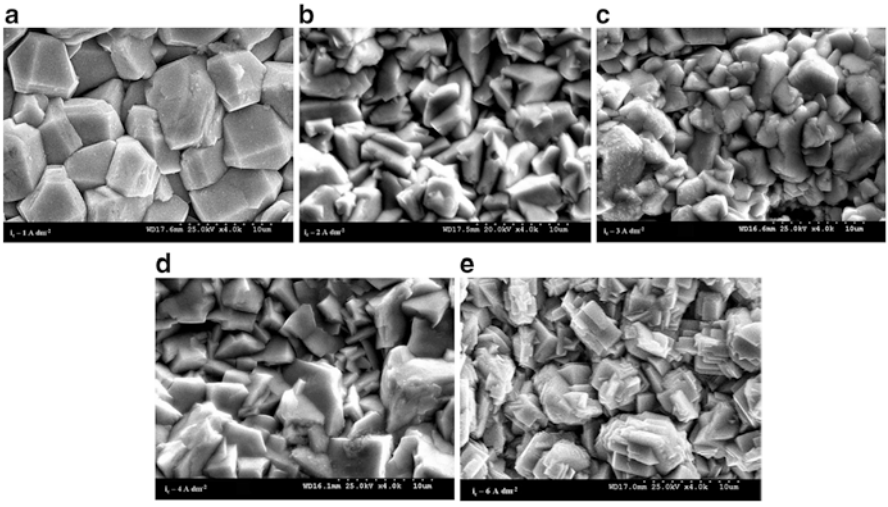

Fig. 7.22 SEM morphologies of Fe–Zn alloy electrodeposits obtained at different current densities: (**a**) −10 mA cm^{-2}, (**b**) −20 mA cm^{-2}, (**c**) −30 mA cm^{-2}, (**d**) −40 mA cm^{-2}, and (**e**) −60 mA cm^{-2} (Reprinted from Ref. [26] with kind permission from Springer)

of the bath used for this study was $ZnSO_4 \cdot 7H_2O$, 0.28 M; $FeSO_4(NH_4)_2SO_4 \cdot 6H_2O$, 0.41 M; and KCl, 1.07 M. Alloys were electrodeposited at different current densities from −10 mA cm^{-2} to −80 mA cm^{-2} and the amount of Fe changed from 6 to 38 wt. % Fe.

Morphology of the Fe–Zn Alloy

SEM images of electrodeposits obtained at different current densities are presented in Fig. 7.22. It could be observed that the electrodeposits morphology was influenced by the alloy composition. Three types of morphologies were observed. For Zn-rich alloy (<10 wt. % Fe content, $i = -10$ mA cm^{-2}), distorted hexagonal morphology was detected. For an alloy with optimum (10–25 wt. %) Fe content, triangular pyramidal morphology ($i = -20$ to -40 mA cm^{-2}) was observed. Relatively smooth and compact electrodeposit with fine-grained morphology (with an Fe content of ≈17 wt. %) was observed at $i = -30$ mA cm^{-2}. Coarser electrodeposits with stacked platelet columnar morphology were produced at cathodic current densities above $i = -50$ mA cm^{-2} (Fe content >25 wt. %). Reduction of crystallite size at $i = -30$ mA cm^{-2} indicates that the nucleation rate was higher than the grain growth rate. This indicates that the overall electrodeposition rate was predominantly controlled by charge-transfer processes rather than mass-transfer processes. But at higher cathodic current densities (above -50 mA cm^{-2}), the overall electrodeposition rate was controlled by mass-transfer limitations particularly for Zn. So the grain growth rate was higher than the nucleation rate and this leads to the formation of coarser morphology enriched with Fe [26].

Electrodeposition of the Fe–Ni Alloy

Fe–Ni alloys (both metals belong to inert ones) were electrodeposited under galvanostatic conditions on the steel substrate for durations 25, 50, and 100 min [27]. The amount of Fe in the electrodeposit was varied by changing the Ni^{2+}/Fe^{2+} ratio in the solution containing constant concentration of $NiCl_2 \cdot 6H_2O$ (23.5 g dm^{-3}), different concentrations of $FeCl_2 \cdot 6H_2O$ (1.0, 1.5, and 2.1 g dm^{-3}), and 20.0 g dm^{-3} H_3BO_3. The plating took place at a constant stirring rate (RPM = 500), by applying current density $i = -20$ mA cm^{-2}. The pH 2 was kept by adding a few drops of sulfuric acid.

Morphology of the Fe–Ni Alloy

Morphology of the Fe–Ni alloys electrodeposited at different Ni^{2+}/Fe^{2+} mass ratios is presented in Fig. 7.23. Figure 7.23a, for sample of Ni^{2+}/Fe^{2+} mass ratio 20.7, displayed a typical elliptical particles shape, with the larger particles growing preferentially out of the surface. By increasing the Fe content (Fig. 7.23b), electrodeposits showed clusters of spherical fine particles embedded in elongated coarse ones with appearance of grain boundaries. For samples prepared at the lowest Ni^{2+}/Fe^{2+} mass ratio of 9.8 (Fig. 7.23c), the microstructure was made of flattened areas containing very fine particles distributed all over the surface. The increase of electrodeposition time had no influence on the appearance of the Fe–Ni alloy electrodeposits.

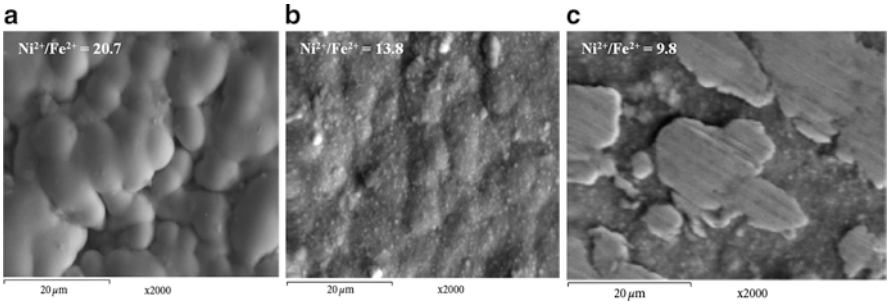

Fig. 7.23 SEM of electrodeposited Ni base layers at current density -20 mA cm^{-2} and deposition time 25 min. as a function of Ni^{2+}/Fe^{2+} mass ratio in the electrolytic bath (Reprinted from Ref. [27] with permission from Hindawi Publishing Corporation)

7.2.2.5 Induced Codeposition

Although it has been shown that Mo, W, Ti, and Ge could not be separately electrodeposited from aqueous solutions, it was discovered that they could be codeposited with the iron-group metals (Fe,Ni,Co) in the presence of appropriate complexing agents. This type of alloy electrodeposition was defined by Brenner [3] as induced codeposition.

Electrodeposition of the Mo–Ni Alloy

In most of the papers concerning the process of induced codeposition of Mo and Ni, where Mo was present in the form of molybdate ion (MoO_4^{2-}), it was assumed that both metals were reduced to a metallic state, producing a Mo–Ni alloy coating. The most probable mechanism of alloy electrodeposition was proposed by Podlaha and Landolt [28–30] and Marlot et al. [31]. Their investigations were performed under controlled mass-transport conditions (rotating cylinder electrode). It was shown that mass-transport control is an important factor for induced codeposition process. In a Ni-rich electrolyte, Mo deposition was mass-transport limited and the alloy composition was strongly influenced by the electrode rotation rate, while in a Mo-rich electrolyte, the rate of Mo electrodeposition was limited by the flux of nickel ions and alloy composition was independent of hydrodynamic effects [28]. The model assumed that Ni electrodeposition occurred on the surface not covered by the molybdate reaction intermediate, by direct reduction of Ni species (all of them being complex of Ni^{2+} cations with the citrate anions) independently on the molybdate reaction, which could occur only in the presence of Ni species [28–31]. The electrodeposition of Mo–Ni alloy was described by following reduction reactions [29]:

$$[Ni(C_6H_5O_7)]^- + 2e^- \rightarrow Ni(s) + (C_6H_5O_7)^{-3} \tag{7.16}$$

$$MoO_4^{-2} + [Ni(C_6H_5O_7)]^- + 2H_2O + 2e^- \rightarrow [Ni(C_6H_5O_7)MoO_2]_{ads}^- + 4OH^- \quad (7.17)$$

$$[Ni(C_6H_5O_7)MoO_2]_{ads}^- + 2H_2O + 4e^- \rightarrow Mo(s) + [Ni(C_6H_5O_7)]^- + 4OH^- \quad (7.18)$$

$$H_2O + e^- \rightarrow \tfrac{1}{2} H_2 + OH^- \quad (7.19)$$

These reactions were postulated with an assumption that the alloy electrodeposition was always accompanied by the simultaneous hydrogen evolution (reaction (7.19)). This model has been confirmed by in situ surface Raman spectroscopic studies, by revealing existence of adsorbed intermediate $[Ni(C_6H_5O_7)MoO_2]_{ads}^-$ at the electrode surface [32].

It was later shown for the Mo–Ni–O powder electrodeposition [33] that this mechanism is only partially correct and that among metallic Ni and Mo, the MoO_3 phase is also electrodeposited. Taking into account that NiO, MoO_3, and $MoNi_4$ phases were detected in as-deposited samples by TEM, it was obvious that the mechanism of alloy electrodeposition similar to the one presented by Eqs. (7.16, 7.17, 7.18, and 7.19) could be applied for the formation of $MoNi_4$ phase only, since it assumed complete reduction of both metal ions. By the analogy with the mechanism proposed by Podlaha and Landolt [28–30], it was suggested that the $MoNi_4$ phase could be formed by the following mechanism [34]:

$$\left[Ni(NH_3)_3\right]^{2+} + 2e^- \rightarrow Ni(s) + 3NH_3 \quad (7.20)$$

$$MoO_4^{2-} + \left[Ni(NH_3)_3\right]^{2+} + 2H_2O + 2e^- \rightarrow \left[Ni(NH_3)_3MoO_2\right]_{ads}^{2+} + 4OH^- \quad (7.21)$$

$$\left[Ni(NH_3)_3MoO_2\right]_{ads}^{2+} + 2H_2O + 4e^- \rightarrow Mo(s) + \left[Ni(NH_3)_3\right]^{2+} + 4OH^- \quad (7.22)$$

with both metals being reduced to a metallic state, Mo(s) and Ni(s).

The most probable mechanism for the MoO_3 phase formation was [34].

$$MoO_4^{2-} + \left[Ni(NH_3)_3\right]^{2+} + 2H_2O + 2e^- \rightarrow MoO_3 + Ni(s) + 3NH_3 + 2OH^- \quad (7.23)$$

Morphology of the Mo–Ni Alloy

Typical nodular morphology of the Mo–Ni alloy surface [35] is shown in Fig. 7.24a, while cross section (Fig. 7.24b) revealed the presence of large cracks in the electrodeposit [36]. Such behavior was characteristic for all Mo–Ni alloys independently of the solution composition and applied current density.

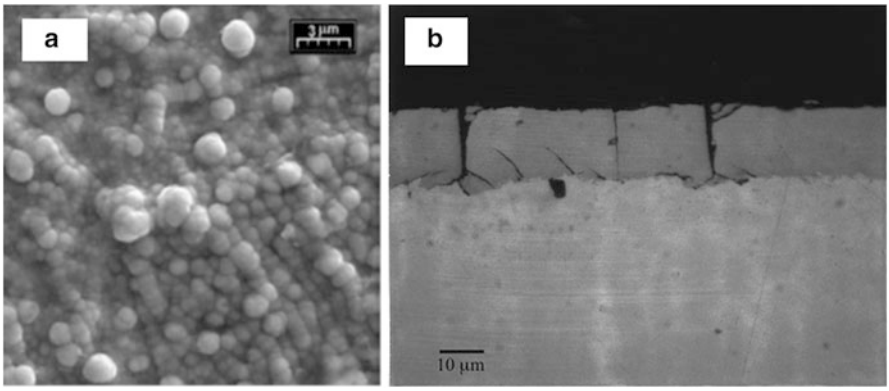

Fig. 7.24 Typical surface morphology (**a**) and cross section (**b**) of the Ni–Mo electrodeposits (**a** – reprinted from Ref. [35] with the permission of Elsevier; **b** – reprinted from Ref. [36] with permission from the International Association of Hydrogen Energy)

Electrodeposition of the Fe–Mo Alloy

The Fe–Mo alloy coatings were electrodeposited onto mild steel substrate from the solution containing $FeCl_3$, Na_2MoO_4, $Na_4P_2O_7$, and $NaHCO_3$, pH 9.3 [37]. Depending on the concentrations of $FeCl_3$, $Na_4P_2O_7$, and Na_2MoO_4, as well as the applied current density, the wt. % of Mo in the coatings (approximate thickness 20 µm) changed from about 45 wt. % to about 70 wt. %, while the current efficiency (η_i) varied from about 10 to 50 %, as shown in Fig. 7.25. It should be stated that in all samples certain (in some cases significant) amount of oxygen has been detected, but this was neglected assuming that the mechanism for induced codeposition defined by Eqs. (7.16, 7.17, 7.18, and 7.19) is operative and, accordingly, only percentages of Fe and Mo were taken into account [37].

Morphology of the Fe–Mo Alloy

Typical morphology of the coatings electrodeposited at different current densities is presented in Fig. 7.26, characterized with nodular surface and large cracks. By the EDS analysis of the Fe–Mo alloy surfaces, it was found that their composition depends on the electrodeposition current density, as shown in Table 7.3. Considering these results, it appeared that the amount of MoO_3 in the electrodeposit decreased with the increase of the electrodeposition current density (lower percentage of oxygen), indicating that the mechanism predicted by Eqs. (7.16, 7.17, and 7.18) and (7.20, 7.21, and 7.22) for Ni–Mo prevailed at higher current densities, while the mechanism for MoO_3 formation (Eq. (7.23) prevailed at lower current densities of Fe–Mo alloy electrodeposition [38].

The cross section of the Fe–Mo alloy electrodeposited at $i = -100$ mA cm^{-2} is shown in Fig. 7.27. All characteristics of the morphology are seen (nodules and cracks) on the cross section (a, b). Distribution of the Fe and Mo in the

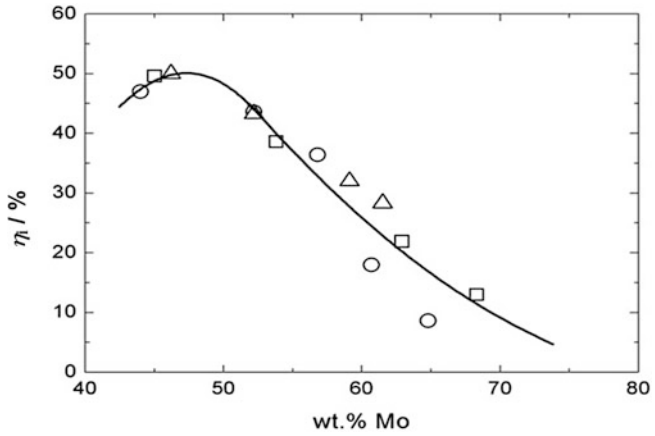

Fig. 7.25 Dependence of η_i on Fe–Mo alloy composition (wt. % Mo), (○) the influence of the $Na_4P_2O_7$ concentration, (□) the influence of the $FeCl_3$ concentration, and (Δ) the influence of the current density for alloy electrodeposition (Reprinted from Ref. [5] with kind permission from Springer)

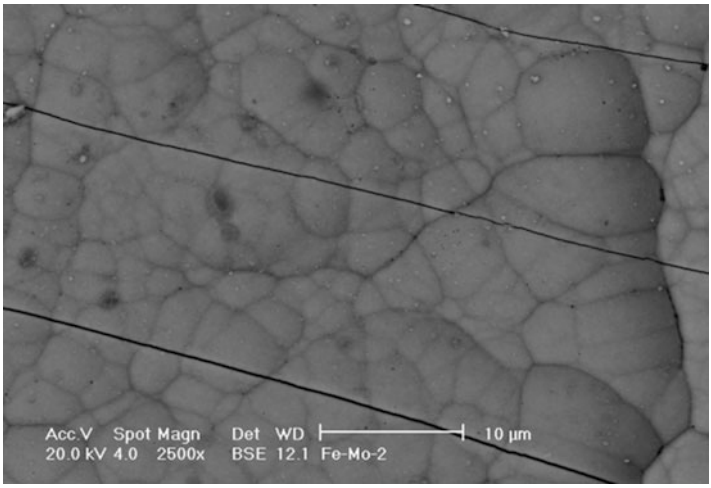

Fig. 7.26 Typical morphology of the Fe–Mo alloy coatings electrodeposited at different current densities (Reprinted from Ref. [5] with kind permission from Springer)

Table 7.3 Composition of the Fe–Mo alloy surfaces, obtained by the EDS analysis, as a function of the electrodeposition current density

i_d/mA·cm^{-2}	at. % O	at. % Mo	at. % Fe
−20	61.20	17.51	21.29
−50	34.05	27.08	38.87
−100	25.80	25.24	48.96

Reprinted from Ref. [5] with kind permission from Springer

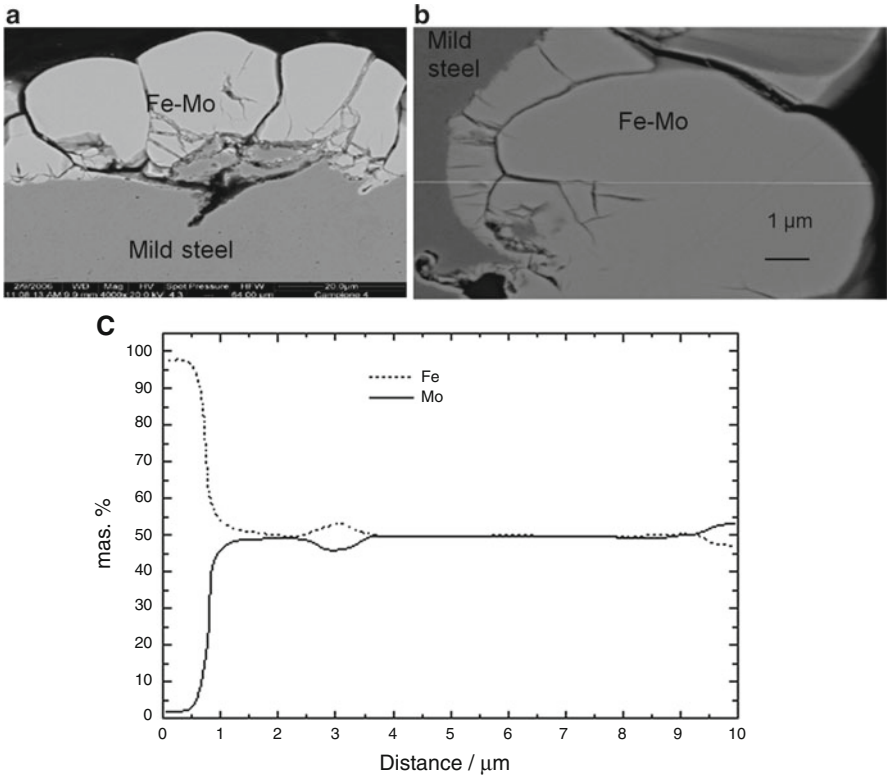

Fig. 7.27 Cross section of the Fe–Mo alloy coating electrodeposited at $i = -100$ mA cm^{-2}, (**a**, **b**). Distribution of the Fe and Mo metals over the electrodeposit obtained by linear EDS analysis (**c**) for sample shown in (**b**) (Reprinted from Ref. [39] with the permission of the Institute for Multidisciplinary Research University of Belgrade)

electrodeposit (neglecting oxygen), obtained by the linear EDS analysis, is presented in Fig. 7.27c, showing uniform distribution of both metals over the entire thickness of the electrodeposit [39].

7.2.3 Specific Structural Phenomena in Electrodeposition of Alloys

Concerning miscibility between the metal constituents of an alloy, all types of alloys could be obtained by electrodeposition: eutectic-type alloys, solid solution-type alloys, alloys with intermediate phases, and/or intermetallic compounds [1]. According to Krastev and Dobrovolska [40], self-organization phenomena during the electrodeposition of alloys, resulting in pattern and spatiotemporal structure

formation on the surface of the coatings, are a consequence of the distribution of different phases in the coating, as well as on its surface, since the properties of heterogeneous alloy coatings are a mixture of the properties of the different phases present in the coatings.

In some cases, the electrodeposition of alloys is accompanied by electrochemical instabilities resulting in current or potential oscillations. This phenomenon was a subject of several review papers [41–43], being explained on the basis of autocatalytic processes, negative electric resistance of the system, etc. Usually, spontaneous formation of layered structures without applying external electrical pulses is a result of oscillatory processes. Such electrodeposits are observed in many systems [3, 44–47]. Multilayered structures could also be obtained by certain current regimes (see Sect. 7.3). In some cases, ordered distribution of the different phases of the heterogeneous alloy coating could be observed, being expressed as spatiotemporal structures.

7.2.3.1 Spatiotemporal Structures in Electrodeposited Alloys

The first spatiotemporal structure was observed in 1938 by Raub and Schall [48] in the system Ag–In. According to their observation, the transition from chaotically distributed phases of the alloy into well-defined periodic spiral structures was caused by the fact that the In-rich phase sometimes forms well-defined crystallization spirals on the surface of the Ag-rich alloy coating. About 50 years later, similar structure formation was observed during electrodeposition of Ag–Sb alloys on Cu substrates in non-agitated electrolytes [49]. At higher contents of Sb, the transition of the α-phase (solid solution of Sb in Ag) of the electrodeposit into a heterogeneous mixture of different textured phases of this alloy system is observed [50]. It was concluded that well-expressed spatiotemporal structures appear in the transition region of the α-phase into hexagonal ξ-phase. An example of the surface of the Ag–Sb coating with spatiotemporal structures is shown in Fig. 7.28a, while in Fig. 7.28b, an example of spatiotemporal structures for the Co–In alloy is shown [51].

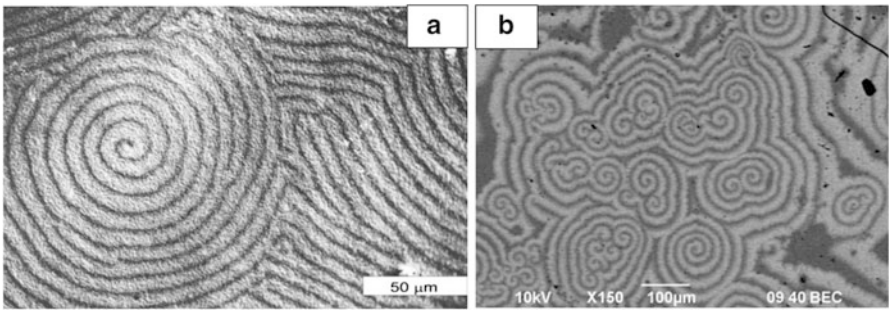

Fig. 7.28 Spatiotemporal structures obtained in the system Ag–Sb (**a**) and Co–In (**b**) (**a** – reprinted from Ref. [40] with kind permission from Springer; **b** – reprinted from Ref. [51] with kind permission from Springer)

The oscillations observed in the Ag–Sb electrodeposition system were found to correspond to the formation of coarse travelling waves consisting of phases with different Sb content and their propagation in front of the Haber–Luggin capillary, leading to the formation of layered structures visible in the cross sections of the electrodeposit [47]. At more negative potentials, the waves become finer, a certain number of them cover the cathode surface in front of the capillary, and further oscillations cannot be registered with this configuration of the capillary. In this case, the formation of smaller waves, spirals with different number of arms, and target patterns is microscopically observed. The electrodeposition of Sb on its own substrate is easier than the one on the Ag substrate [52], ensuring necessary autocatalytic step for the appearance of the self-organization phenomenon. It is believed that the movement of the coarse waves in vertical direction on the electrode surface takes place due to the upwards flow of the electrolyte as a consequence of the natural convection, which seems to be one of the crucial factors for the appearance of this instability and the periodical pattern formation. This hypothesis was confirmed by experiments in a strong magnetic field (5 T) [52] where the natural convection was suppressed by the magnetohydrodynamic flow in horizontal direction at an appropriate orientation of the cell to the magnetic field. The results showed that the waves are situated perpendicularly to the flow of the electrolyte and moves in the direction of the flow. The observed instability was called "flow-induced electrochemical instability" [52]. The appropriate combination of the different factors during electrodeposition and the resulting velocity of the wave propagation probably play a very important role in the formation of the periodic structures as well. The waves in the case of the Ag–Sb spatiotemporal structures move with a velocity of several micrometers per second, and the rotation speed of the spiral structures is of about 8° per second [40].

7.2.4 Electrodeposition of Alloys with Periodically Changing Currents

7.2.4.1 Electrodeposited Au–Sn Alloy

Au–Sn eutectic solders ("hard solder" with superior mechanical and thermal properties relative to "soft" solders, such as the Pb–Sn system) are commonly used in the optoelectronic and microelectronic industries for chip bonding to dies [53]. In order to avoid the use of cyanide solutions, chloride solutions were developed at the beginning of 1990. The most stable one was found to be solution containing [53] 200 g dm^{-3} $(NH_4)_3C_6H_5O_7$, 5 g dm^{-3} $KAuCl_4$, 60 g dm^{-3} Na_2SO_3, 15 g dm^{-3} L-ascorbic acid, and 5 g dm^{-3} $SnCl_2 \times 2H_2O$. This solution was used to investigate the morphology of the electrodeposits obtained by direct (DC) and pulsating (PC) current regimes. Taking into account that Au belongs to the intermediate metals, while Sn belongs to normal metals, it could be expected that PC regimes would produce less rough electrodeposits. Due to low concentrations of Au and Sn

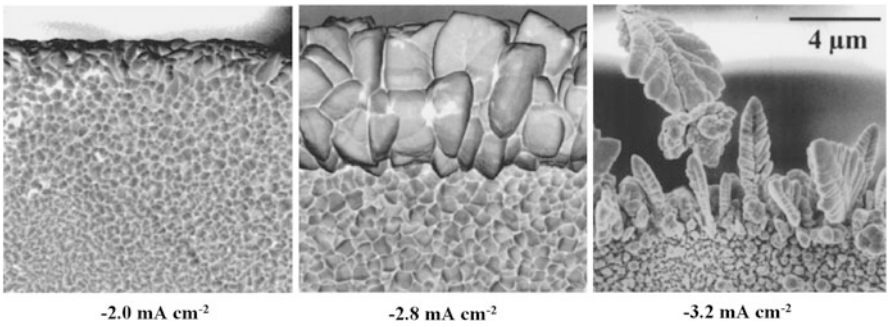

Fig. 7.29 SEMSE images showing edge effects in PC plating at different average current densities. The on-time and off-time for PC plating are 2 ms and 8 ms, respectively (Reprinted from Ref. [54] with kind permission from Springer)

ions, small values of average cathodic current densities (up to -3.4 mA cm^{-2}) were used in DC and PC plating, varying on- and off-times, and average current density in PC plating. Electrodeposits obtained at low current densities (from -1.6 to -2.0 mA cm^{-2}) were similar for both types of plating with practically no influence on their microstructure. At slightly higher current densities (from -2.0 to -3.2 mA cm^{-2}), both DC and PC electrodeposits showed a tendency toward coarser microstructures, with this effect being more pronounced for DC electrodeposits. The cathodes were either InP or Si wafers, coated with Ti (25 nm)/Au (250 nm) blanket metallizations. Wafers were sectioned into smaller pieces, each having an exposed area ~1 cm^2 defined by stop-off lacquer. The increase of the average current density in PC regime caused coarser grain size all over the electrodeposit, while this increase was the most pronounced on the appearance of the edge of electrodeposit, as shown in Fig. 7.29. The actual current density at the edge is higher than the average current density, approaching the limiting current density and the electrodeposits at the edge exhibit microstructures characteristic of limiting current conditions (coarse grains and even dendritic growth, $i = -3.2$ mA cm^{-2}) [54].

The on-time period showed the most significant effect on the microstructure characteristics of the Au–Sn electrodeposits. As can be seen on the SEM micrographs presented in Fig. 7.30, the sample electrodeposited with 1 ms on-time possessed much finer microstructure than the other coatings. This is caused by two factors: composition and grain size. High Au content or low Sn content (16.7 at.%) relative to the others (content of Sn higher than 33 at.%) and lower roughness, which was found to increase with increasing on-time. At longer on-times, the average current density increases leading to thicker and coarser electrodeposits. At 4 ms of on-time, the microstructure approaches that obtained from DC plating [54]. Cleaved cross sections of the electrodeposits in Fig. 7.30 are shown in Fig. 7.31. The 1 ms on-time sample exhibits ductile fracture, most probably due to its high Au content. Electrodeposits obtained at 2 and 3 ms of on-time are dense and uniform and adhere well to the substrate, with the microstructures similar to typical solidified cast

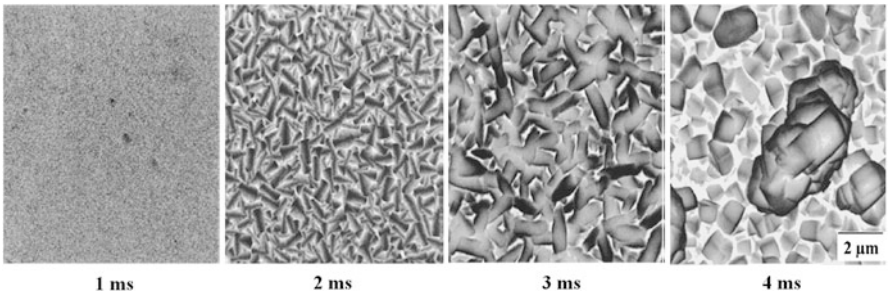

Fig. 7.30 SEMSE images of electrodeposits obtained at different on-times, with a constant peak current density of -10 mA cm^{-2} and an off-time of 8 ms (Reprinted from Ref. [54] with kind permission from Springer)

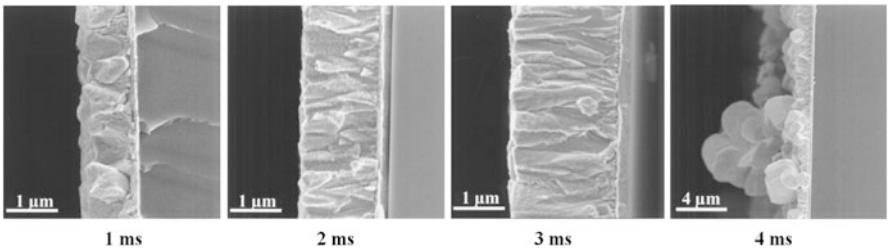

Fig. 7.31 SEM cleaved cross-sectional images of electrodeposits obtained at different on-times, with a constant peak current density of -10 mA cm^{-2} and an off-time of 8 ms (Reprinted from Ref. [54] with kind permission from Springer)

structures (the initial electrodeposit is fine grained and subsequent grains growing in a columnar manner). The 4 ms on-time sample is very rough – its thickness varies from 1.4 to 8.9 μm – which is due to the high average current density (-3.3 mA cm^{-2}) approaching the limiting current density. Generally speaking, on-times of 1–3 ms produce suitable microstructures and reasonable plating rates (0.7–1.7 μm h^{-1}). Higher plating rates could be achieved by increasing the Au and Sn contents in the plating bath (increasing the limiting current density).

7.2.4.2 Electrodeposited Co–Cu Alloy

This is one example of codeposition of one intermediate (Cu) and one inert (Co) metal. The electrolyte for electrodeposition [55] contained 0.7 M $CoSO_4 \cdot 7H_2O$, 0.025 M $CuSO_4 \cdot 5H_2O$, 0.18 M $Na_3C_6H_5O_7 \cdot 2H_2O$, and 1:50 parts of 0.04 % premixed FC99 fluorinated surfactant from 3 M® with the pH 4.3. The effect of pulse off-time on the phase distribution of Co–Cu alloys pulse-plated on the IrRDE (inverted recessed rotating disk electrodes) was studied in order to get additional information on the role of the displacement reaction.

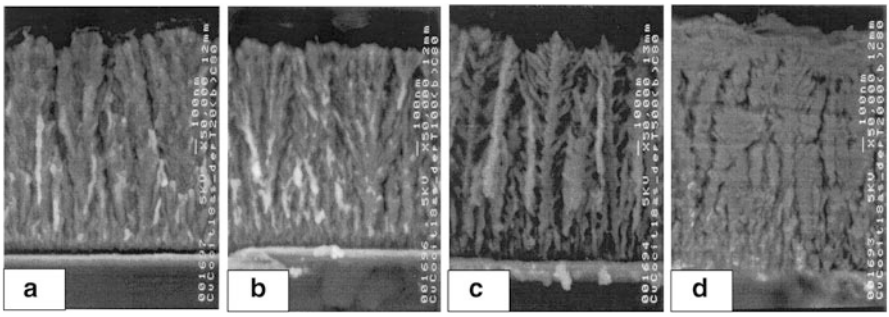

Fig. 7.32 SEM pictures of Co–Cu alloy electrodeposit cross sections after selective chemical etching of the Cu phase. Bright parts represent the Co-rich phase, while dark parts represent the etched Cu phase. Off-time (ms): 16 (**a**), 80 (**b**), 400 (**c**), and 1600 (**d**) (Reprinted from Ref. [55] with the permission of Elsevier)

The experimental conditions were pulse off-times 16, 80, 400, and 1600 s, duty cycle 0.2, pulse current density $i_{on} = -100$ mA cm^{-2}, current density during off-time $i_{off} = -0.2$ mA cm^{-2}, and RPM = 1400. Under such hydrodynamic conditions, a limiting current density for copper electrodeposition was $i_L(Cu) = -9.7$ mA cm^{-2}. The number of cycles (depending on the on-time and off-time) was 11022, 2204, 441, and 110, respectively, in order to obtain approximately 1.3 mm thick electrodeposits. The SEMs of etched cross sections presented in Fig. 7.32 illustrate the phase distribution obtained in the experiments. Except for the electrodeposit shown in Fig. 7.32d, which had the lowest Cu content, the electrodeposits exhibited a columnar structure. The Co alloy columns apparently go through the entire electrodeposit, indicating that atoms are added to existing growth sites in each phase [55].

7.3 Multilayered Structures

7.3.1 Introduction

According to the theory of composite systems [56], the existence of intermediate layer between two metals is inevitable in multilayered laminar metal structures. The thickness of the intermediate layer is usually of the order of couple atomic layers, and the parameters of the system (concentration of individual metals, crystal structure, Young's modulus, density, coefficient of thermal expansion, etc.) change from one layer to another. Usually such intermediate layer is composed of two layers of solid solutions and one layer of intermetallic compound, as it is schematically presented in Fig. 7.33.

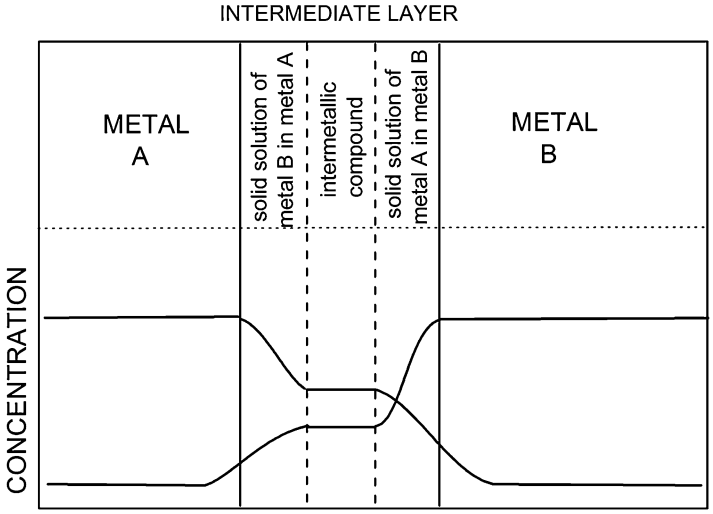

Fig. 7.33 Schematic representation of the intermediate layer in multilayered laminar metal structures (Reprinted from Ref. [5] with kind permission from Springer)

By using appropriate techniques for the formation of such structures (chemical or physical evaporation, electrodeposition, etc.), it is possible to achieve high value of total surface area of the intermediate layer amounting to 3000 cm^2 cm^{-3}. Accordingly, the larger the surface of the intermediate layer, the higher the difference in the properties of the multilayered laminar metal structure (higher values of Young's modulus, hardness, tensile strength, etc.) [56]. Taking into account that the electrodeposition of such structures is the cheapest technique, its advantage over the other techniques is obvious.

It should be emphasized here that multilayered laminar metal structures could be obtained by electrodeposition of individual metal layers from separate baths, which is a time-consuming process. On the other side, it is possible to obtain such electrodeposit from one bath containing ions of both metals by appropriate choice of metal ion concentration and applied current density. Hence, by appropriate choice of electrodeposition conditions, one can adjust the composition and the thickness of each layer and, accordingly, properties of such structures.

7.3.2 Electrodeposition of Laminar Metal Structures

As already stated above, multilayered laminar metal structures could be obtained by electrodeposition of individual metal layers from separate baths or from one bath containing ions of both metals. Only the second case is of interest for this chapter and such conditions will be discussed [1, 5].

7.3.2.1 Spontaneous Formation of Layered Deposits

In the investigations of electrodeposition of alloys, laminar metal structures, parallel to the cathode surface, were observed in quite a few instances [1, 5]. This phenomenon has been accompanied with the fluctuations of potential ranging from 0.1 mV to 0.1 V depending on the system and applied current density. Any fluctuations of periodic nature (oscillations) must be the consequence of superposition of two counteracting processes. Accordingly, this phenomenon could be explained in a following way: At the beginning of the process under galvanostatic conditions, the rate of electrodeposition of the more noble metal is sufficient for its nuclei to be formed and its grains to grow. However, after some time, due to depletion of the diffusion layer, the concentration of the ions of the more noble metal at the cathode surface becomes practically zero, and the discharge of the ions of the less noble metal must compensate for the decrease of the partial current density of the more noble metal. This requires a certain increase in cathodic overpotential and nucleation and growth of the less noble metal mainly. After some time, the concentration of the ions of the more noble metal at the cathode surface recovers to the point where its nucleation can start again, causing decrease of the cathodic overpotential and, accordingly, the nucleation and growth of the less noble metal subsides. Hence, the process starts all over again.

7.3.2.2 Formation of Laminar Deposits by Pulsating Current Regimes

Instead of letting laminar metal structures to be formed spontaneously during the alloy electrodeposition, there was significant motivation to obtain well-defined multilayered structures of controlled compositions and thicknesses of individual layers. Electrodeposition of such structures was first demonstrated by Brenner [3], while Cohen et al. [57] obtained an Ag–Pd alloy with periodically changing composition by alternating the current density and such structure showed improved wear performance of electrical contacts. In order to obtain laminar metal structure with the thickness of individual layers (with the second layer being Cu–Ni alloy with small amount of Ni) of 300 nm in the system Cu–Ni, pulsating regimes were used [58, 59]. It was shown that such structures possessed higher tensile strength [58] and microhardness [59].

In the application of pulsating regimes [57–59], three types of pulses, schematically presented in Fig. 7.34, were used.

The first attempt in theoretical treatment of the variation of the composition of the electrodeposit obtained by pulsating current from a bath containing two different metal ions, using complicated mathematical procedure, was presented in 1985 [60]. The quantitative theory of laminar metal electrodeposition based on fundamental concepts of electrode kinetics, using much simpler mathematical approach, was presented in a series of papers of Despić and co-workers [61–63].

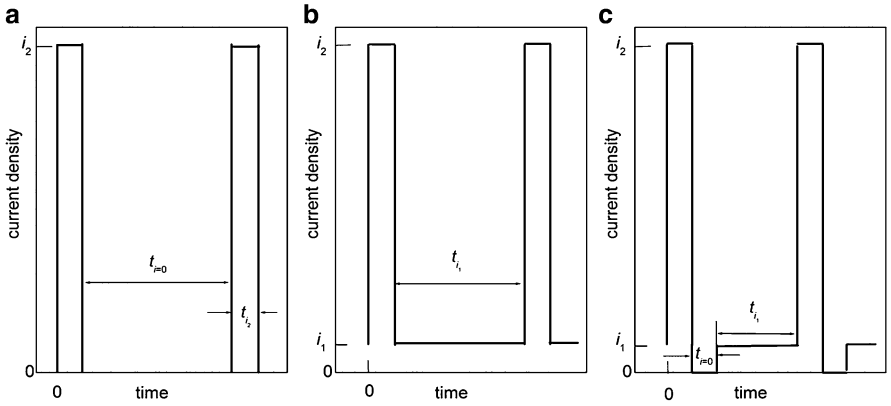

Fig. 7.34 Schematic presentation of pulsating regimes used for electrodeposition of laminar metal structures (Reprinted from Ref. [5] with kind permission from Springer)

Single Current Pulse Regime

For the electrodeposition of laminar metal coatings, two conditions must be fulfilled: (1) The reversible potentials for metals A and B must be sufficiently different so that at a given current density, the less noble one (B) virtually does not electrodeposit during the electrodeposition of the more noble one (A) until complete concentration polarization with respect to ions of metal A takes place; (2) within the duration of the current density pulse, Send's equation [15] for diffusional polarization is obeyed with respect to concentration change, resulting in transition from electrodeposition of metal A to electrodeposition of metal B after well-defined transition time.

Hence, the first layer contains pure metal A and its thickness is, according to Faraday's law, defined by equation

$$d(\mathrm{I}) = \left(\frac{M_\mathrm{A}}{z_\mathrm{A}\rho_\mathrm{A}F}\right) i\tau_\mathrm{A} \tag{7.24}$$

where M_A, ρ_A, and z_A are, respectively, atomic weight, density, and charge on the ions of metal A, and i is the current density in the pulse, while τ_A is the transition time with respect to the ions of metal A. Assuming that the convection and migration of ions of the electrolyte is negligible, τ_A is defined by Send's equation [15]:

$$\tau_\mathrm{A} = \frac{(z_\mathrm{A}F)^2 \pi D_\mathrm{A}}{4}\left(\frac{C_\mathrm{A}^\mathrm{o}}{i}\right)^2 \tag{7.25}$$

where $C_\mathrm{A}{}^\mathrm{o}$ and D_A are, respectively, the bulk concentration and diffusion coefficient of the ions of metal A. Introducing Eq. (7.25) into Eq. (7.24) and rearranging one obtains

$$\frac{\left(C_{\mathrm{A}}^{\mathrm{o}}\right)^2}{i} = \frac{4\rho_{\mathrm{A}}}{z_{\mathrm{A}}F\pi D_{\mathrm{A}}M_{\mathrm{A}}}\mathrm{d}(I) \tag{7.26}$$

Considering Eq. (7.26), it could be concluded that desired thickness of the layer of metal A could be achieved by proper choice of metal ion concentration and the current density of the pulse.

Taking into account that Sand's equation is valid only as long as the change of concentration occurs within a stagnant layer undisturbed by convection and introducing the Nernst diffusion layer boundary δ and hydrodynamic layer boundary Δh, the minimum current density that must be applied in the first pulse for electrodeposition of the second layer to take place is given by

$$i^{\min} = \frac{z_{\mathrm{A}}F\pi D_{\mathrm{A}}}{2\Delta h}C_{\mathrm{A}}^{\mathrm{o}} \tag{7.27}$$

and, accordingly, by introducing Eq. (7.26) into Eq. (7.27), the maximum achievable thickness of the first layer (metal A) is

$$\mathrm{d}(I)^{\max} = \frac{M_{\mathrm{A}}C_{\mathrm{A}}^{\mathrm{o}}\Delta h}{2\rho_{\mathrm{A}}} \tag{7.28}$$

Electrodeposition of the second layer starts after τ_{A} is reached and is accompanied by sudden change of potential to the reversible potential of metal B electrodeposition plus the overpotential for its electrodeposition [1, 5].

The shape of the potential versus time (E vs. t) response in such a case depends on the property of the alloy and its constituents in the investigated solution. Two situations could be considered: (a) replacement reaction takes place during the off-time ($i = 0$) period; (b) replacement reaction does not take place during the off-time ($i = 0$) period.

If the difference between the reversible potentials of metals A and B is sufficient, and the constituents of the alloy do not mix in the solid state (eutectic-type alloy), and/or electrodeposition/dissolution of metal B is reversible (case a), replacement reaction must take place during the off-time ($i = 0$). Such a case is schematically presented in Fig. 7.35. The current density change is presented in (a), while corresponding potential change is presented in (b). As can be seen, after reaching τ_{A}, metal A continues to electrodeposit but at a decreasing partial current density (actually by its diffusion limiting current density, $i_{\mathrm{d}}(\mathrm{A}) = i_{\mathrm{L}}(\mathrm{A})$), while the partial current density of the metal B, $i_{\mathrm{d}}(\mathrm{B})$, increases to make a constant current density of the pulse, i_{d}. If the concentration of ions of metal B is much larger than that of the metal A, the growth of the second layer could be virtually unlimited and the content of metal A in the second layer will continuously decrease with the thickness of the second layer (following the decrease of $i_{\mathrm{d}}(\mathrm{A})$). Corresponding potential response, schematically presented in (b), is characterized by a sudden increase of cathodic potential to the value higher than $E_{\mathrm{r}}(\mathrm{B})$ at the position of τ_{A}. At the position of the

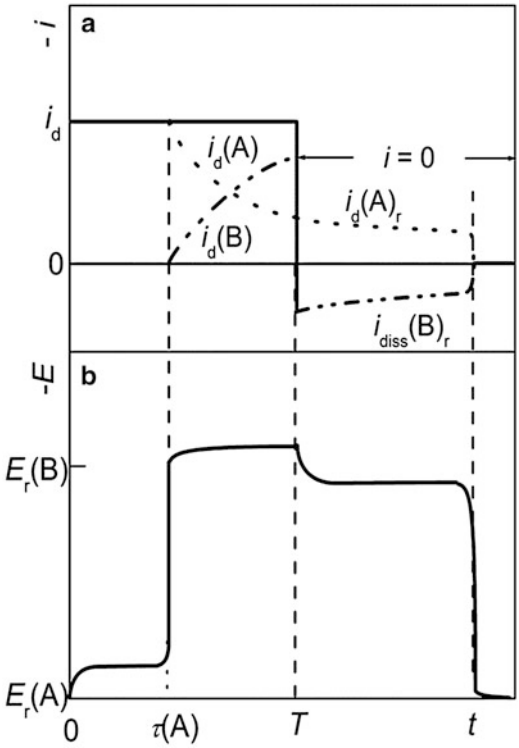

Fig. 7.35 Schematic representation of the partial current density changes (**a**) and corresponding potential response (**b**) during the electrodeposition of two-layer of metals A and A + B by constant current density pulse (i_d) up to time T and during the replacement reaction at $i = 0$. Partial current density for electrodeposition of metal A after reaching τ_A, i_d(A); partial current density for electrodeposition of metal B after reaching τ_A, i_d(B); partial current density for electrodeposition of metal A during the replacement reaction, $i_d(A)_r$; partial current density for dissolution of metal B during the replacement reaction, $i_{diss}(B)_r$ (Reprinted from Ref. [5] with kind permission from Springer)

end of the current pulse (T) and the beginning of the current density off period ($i = 0$), replacement reaction will take place. The electrodeposition of metal A will continue with $i_d(A) = i_L(A) = i_d(A)_r$, while, in order to keep total current density at zero, the less noble metal B will start to dissolve with the positive partial current density $i_{diss}(B)_r$ equal to that of metal A electrodeposition. Once this process is finished, either due to dissolution of the whole amount of metal B in the second layer or prevention of its dissolution for some reasons (e.g., at some places of a second layer atoms of metal B become covered with a monolayer of metal A), the current density $i_{diss}(B)_r$ will drop to zero and corresponding potential to the value of E_r(A) [1, 5].

Although the replacement reactions have extensively been studied [64], the only example for such reaction in the layered electrodeposits was demonstrated for the system Cu–Pb [1, 5, 61]. A two-layer structure, composed of a first layer of pure Cu

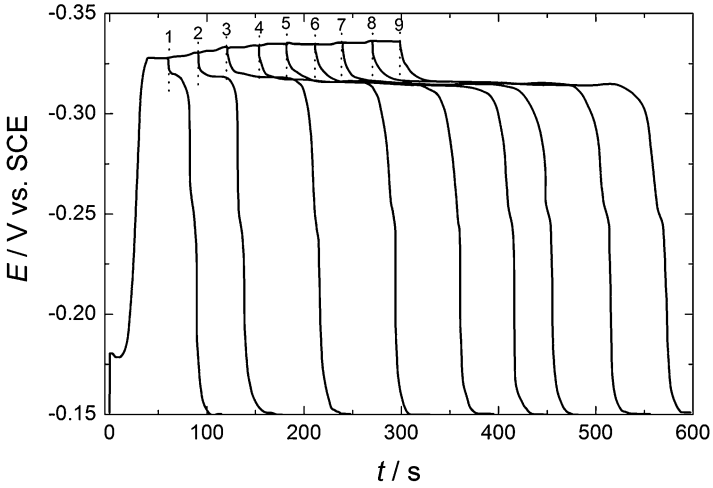

Fig. 7.36 Potential responses recorded during constant current density $i_d = -1$ mA cm^{-2} pulse trains on a stationary glassy carbon electrode from a solution containing 0.01 M Cu $(CH_3COO)_2 + 0.01$ M $Pb(CH_3COO)_2 + 1$ M HBF_4. After the electrodeposition, zero current density ($i = 0$) was applied (positions marked in the figure with 1–9) (Reprinted from Ref. [5] with kind permission from Springer)

and a second layer of Cu–Pb alloy, has been electrodeposited at a constant current density $i_d = -1$ mA cm^{-2} for different times (from 60 to 300 s) on a stationary glassy carbon electrode [61] from a solution containing 0.01 M Cu $(CH_3COO)_2 + 0.01$ M $Pb(CH_3COO)_2 + 1$ M HBF_4. After the electrodeposition, zero current density ($i = 0$) was applied (positions marked in the figure with 1, 2, 3, 4, 5, 6, 7, 8, and 9) and corresponding potential responses are presented in Fig. 7.36. As can be seen after applying zero current density (positions 1–9), the potential remains for some time at a level slightly below the reversible potential of Pb, after which it falls to the potential of Cu. That time is virtually equal to duration of the current density pulse, indicating that the dissolution of Pb from a second layer occurs all the time. When the dissolution process is finished, potential returned to the reversible potential of Cu. By the EDS analysis, it was confirmed that the whole amount of electrodeposited Pb has been dissolved during the off-time periods. Hence, all conditions (*a*) for the replacement reaction to take place were fulfilled: Cu–Pb is eutectic-type alloy and electrodeposition/dissolution of Pb is reversible [1, 5, 61].

If the difference between the reversible potentials of metals A and B is sufficient, and the constituents of the alloy mix in the solid state forming solid solution and a metal B passivates in the electrolyte used (case *b*), replacement reaction will not take place during the off-time ($i = 0$). Such a case is schematically presented in Fig. 7.37. The current density change is presented in (a), while corresponding potential change is presented in (b). During the current density pulse, everything is the same as in a previous case. The absence of replacement reaction is

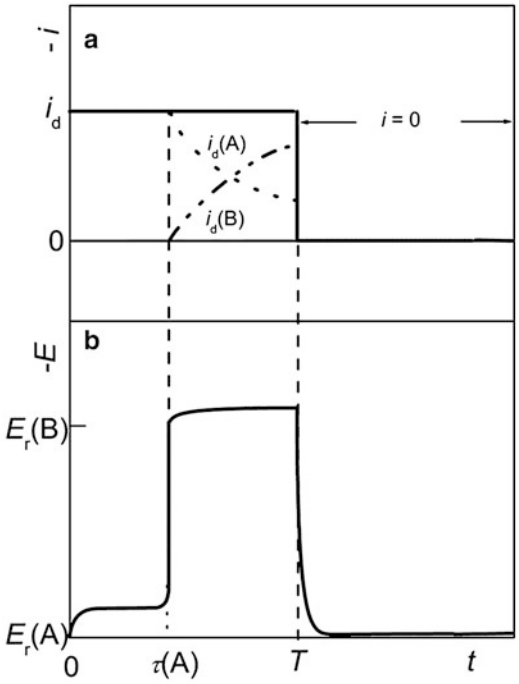

Fig. 7.37 Schematic representation of the partial current density changes (**a**) and corresponding potential response (**b**) during the electrodeposition of two layers of metals A and A + B by constant current density pulse (i_d) up to time T and after, in the absence of the replacement reaction at $i = 0$. Partial current density for electrodeposition of metal A after reaching $\tau_A - i_d(A)$, partial current density for electrodeposition of metal B after reaching $\tau_A - i_d(B)$ (Reprinted from Ref. [5] with kind permission from Springer)

characterized by sudden potential change from $E_r(B)$ to $E_r(A)$ at the position of the end of the current pulse (T) and the beginning of the current density off period ($i = 0$) [5, 58].

Typical example for such behavior is the system Cu–Ni [58, 59, 63, 65, 66]. This system belongs to the solid solution-type alloys, and the dissolution of Ni is prevented by its passivation in the electrolyte for electrodeposition.

Dual Current Pulse Regime

Single current pulse regime imposes serious limitations on both the thickness of the layers of the more noble metal and the content of that metal in the second layer. The application of a dual current pulse scheme was found more suitable for manipulation of the thickness of each layer, as well as the content of the more noble metal in the second layer. The scheme consists of current pulses in two different intensities each. A lower current density $i(I)$ for a certain time period $T(I)$ is followed by a

higher current density i(II) for a period T(II) before the current is interrupted (or the sequence repeated). It can be shown that with such a scheme and proper choice of parameters, any desired thickness of both layers can be achieved and the content of metal A in the second layer can be reduced to a desired level. The process can be improved, in terms of shortening the electrodeposition time of the first layer while maintaining a desired content of metal A in the second layer, by synchronously modulating the hydrodynamic conditions. Such a process can have significant practical value for obtaining bilayers (or multilayers) [1, 5, 62].

In the dual current pulse regime, it is desirable to have

$$C_{\mathrm{B}}^{\mathrm{o}} >> C_{\mathrm{A}}^{\mathrm{o}} \tag{7.29}$$

the best choice being that which satisfies equality

$$\frac{C_{\mathrm{B}}^{\mathrm{o}}}{i(\mathrm{II})} = \frac{C_{\mathrm{A}}^{\mathrm{o}}}{i(\mathrm{I})} \tag{7.30}$$

An attempt was made to electrodeposit two-layer structure composed of pure (first) Cu layer of about 2 μm and the second layer of different Cu–Ni alloy compositions of a thickness of about 12 μm by applying dual current pulse regime presented in Fig. 7.38. The two layers were deposited onto Ag rotating disc electrode (RPM = 1000) from the solution 0.02 M $CuSO_4$ + 2 M $NiSO_4$ + 0.5 M $Na_3C_6H_5O_7$. The value of the current density in the first pulse, i(I), was adjusted at 75 % of the value of the diffusion limiting current density for copper ions at the given concentration and rotation speed [62].

Relatively smooth electrodeposits, consisting of two well-defined layers, were obtained. Results of the EDS analysis of the composition of the second layer (Cu–Ni alloy) of the electrodeposits obtained by the current regimes shown in Fig. 7.38 are compared in Table 7.4 with the composition of the second layer calculated from the current density ratio (c.r.) in the second pulse assuming 100 % current efficiency for alloy electrodeposition, c.r. – $i(\mathrm{Ni})/i(\mathrm{Cu})_{\mathrm{L}}$. Taking into account precision of the EDS analysis, it is seen that a relatively good agreement is obtained.

A multilayer structure consisting of ten relatively thick layers shown in Fig. 7.39 was obtained by the current regime presented in Fig. 7.40.

Presented analysis confirmed that the thickness and the composition of layered electrodeposits could be controlled with sufficient precision [62].

7.3.2.3 Intermediate Layer Detection

Taking into consideration the fact that the intermediate layer in electrodeposited laminar metal structures plays an important role in obtaining improved mechanical and magnetic properties [56], from 1980 to 2000, particular attention has been given to the pulsating regimes which would provide as thin as possible layers (of the

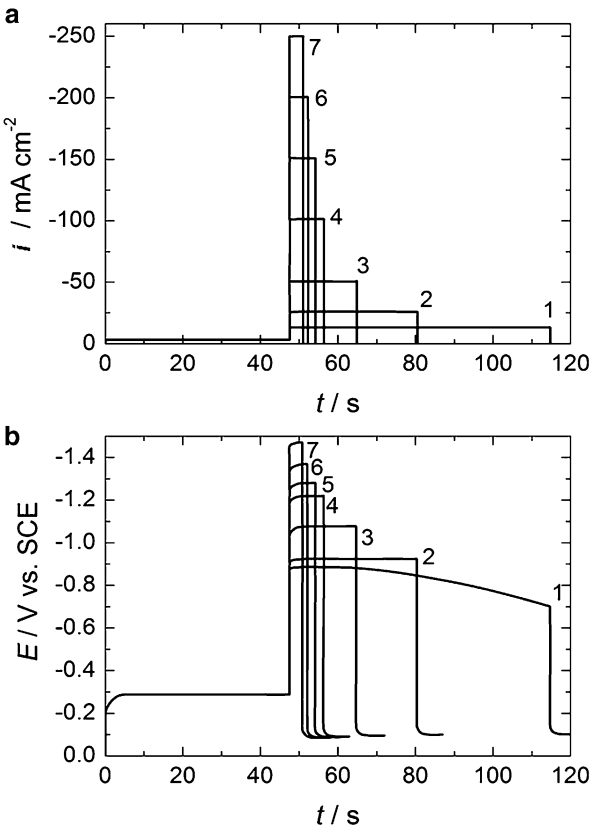

Fig. 7.38 A sequence of high current density pulses (**a**) and corresponding potential responses (**b**) (marked with numbers 1–7) during the formation of two-layer structure composed of a pure (first) Cu layer of about 2 μm and the second layer of different Cu–Ni alloy compositions of a thickness of about 12 μm. The current density ratio, c.r. $-i(\mathrm{Ni})/i(\mathrm{Cu})_L$, for pulse no. 1–2.0, no. 2–5.3, no. 3–13.3, no. 4–27.6, no. 5–36.5, no. 6–56.1, no. 7–61.5 (Reprinted from Ref. [5] with kind permission from Springer)

Table 7.4 The composition of the second layer of the electrodeposits as a function of the current density ratio (c.r.)

		Composition of the second layer			
		EDS analysis		Calculated from c.r.	
Pulse no.	c.r.	at. % Cu	at. % Ni	at. % Cu	at. % Ni
1	2.0	35.4	64.6	33.3	66.7
2	5.3	20.8	79.2	16.0	84.0
3	13.3	7.9	92.1	7.0	93.0
4	27.6	4.9	95.1	3.5	96.5
5	36.5	4.7	95.3	2.7	97.3
6	56.1	3.9	96.1	1.7	98.3
7	61.5	4.2	95.8	1.6	98.4

Reprinted from Ref. [5] with kind permission from Springer

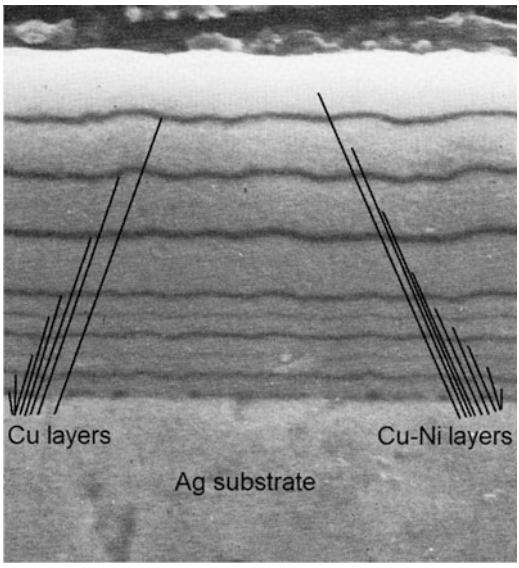

Fig. 7.39 Multilayer structure obtained by the current pulses presented in Fig. 7.40 (Reprinted from Ref. [5] with kind permission from Springer)

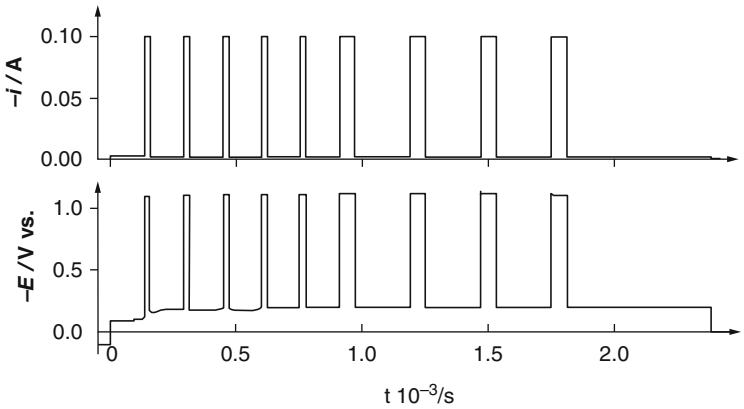

Fig. 7.40 Current density pulses and corresponding potential responses applied for the formation of multilayer structure presented in Fig. 7.39 (Reprinted from Ref. [5] with kind permission from Springer)

order of nanometers) [65–69] in multilayered metal structures, and, accordingly, much higher surface area of the intermediate layer.

In theoretical consideration of multilayer electrodeposition of Cu–Ni alloy under the conditions of convective diffusion [63], it was shown that a constant concentration of Cu in the second layer (Cu–Ni alloy) could be established at different thicknesses of the second layer, depending on the value of the current density of a second pulse and the rotation rate. As the value of the current density in the second pulse increases the thickness at which a constant concentration of Cu could be

established also increases, indicating that the thickness of the intermediate layer also increases, reaching the maximum value of about 150 nm [63]. Unfortunately, this theoretical consideration was not experimentally confirmed. Most of the experimentally confirmed theoretical treatments of the pulsed electrodeposition of multilayered structure have been applied to the Cu–Ni system [70–73]. Equations for partial currents for Cu and Cu–Ni electrodeposition [71] (including the evolution of hydrogen) from a single bath in the case of galvanostatic [70] and potentiostatic [71] electrodeposition of multilayered Cu–Ni coatings under the conditions of convective diffusion were developed. The experimental results were in good agreement with the theoretical predictions. The subject of two papers [72, 73] was the process taking place during the off-time period in pulsed electrodeposition, showing that during the off-time period Cu electrodeposits by a displacement of Ni ("replacement reaction"). Their models were found to agree well with the experimental findings. Hence, the existence of an intermediate layer in these investigations has not been confirmed experimentally.

However, it was shown in the system Cd–Ni [74] that the intermediate layer could be detected by the application of the ALSV technique. Alloy samples used for the ALSV analysis were galvanostatically electrodeposited at the amount of charge of -1 C cm^{-2} in the solution containing 2 M $NiSO_4 + 0.2$ M $Na_3C_6H_5O_7 +$ 0.002 M $CdSO_4$. Pure Ni and pure Cd layers were also electrodeposited galvanostatically at $i_d = -10$ mA cm^{-2} ($Q_d = -1$ C cm^{-2}) from the solutions containing 2 M $Ni(NH_2SO_3)_2 + 0.5$ M H_3BO_3 and 0.5 M $CdSO_4 + 0.01$ M H_2SO_4, respectively. The samples composed of a layer of alloy and a layer of pure Cd on top of the alloy layer, used for the analysis of the intermediate layer existence, were galvanostatically deposited from two different baths: 2 M $NiSO_4 + 0.2$ M $Na_3C_6H_5O_7 +$ 0.002 M $CdSO_4$ and 2 M $Ni(NH_2SO_3)_2 + 0.5$ M $H_3BO_3 + 0.002$ M $CdSO_4$. All samples were electrodeposited onto Au disc electrode at RPM = 1000 and were dissolved in a solution of 1 M NaCl (pH 2) at RPM = 0.

(a) *Intermediate layer between Ni and Cd electrodeposited from a separate baths*: For this purpose, layers of pure Cd and pure Ni were electrodeposited from the appropriate separate baths onto gold disc electrode. To provide normal dissolution of these metals, Ni was first electrodeposited as a more noble metal and a layer of Cd was electrodeposited on top of it. From such electrodeposit, Cd dissolves at about -0.8 to -0.7 V versus SCE, while Ni starts to dissolve at about -0.33 V versus SCE with the peak appearing at about -0.1 V versus SCE.

Hence, to detect an intermediate layer between these two metals, ALSVs of pure Ni and pure Cd dissolution were first recorded. Then, after the electrodeposition of a layer of Cd on top of a layer of Ni, an ALSV of dissolution of such electrodeposit consisting of two metal layers was recorded. Since these two metals make two intermediate phases [8], in the case of interaction between the two layers, one would expect one or two small ALSV peaks, pertaining to the dissolution of either of these phases, between the peaks of dissolution of pure metals. There was no indication, however, of the existence

of any additional ALSV peak even after prolonged thermal treatment (deposit was kept in an atmosphere of purified nitrogen at a temperature of 50 °C for 24 h) of such deposit. Knowing that the ALSV technique is very sensitive and that it is possible to detect clearly a monolayer of metals by this technique, it appeared that in the case of Ni and Cd layers, electrodeposited from a separate baths, no intermediate layer between them has been formed.

(b) *Intermediate layer between Cd–Ni alloy and pure Cd electrodeposited from a single bath*

The system Cd–Ni should be very suitable for the detection of intermediate layer since the ALSVs of Cd–Ni alloy dissolution were seen to be characterized by the existence of two ALSV peaks corresponding to the dissolution of phases β and γ of the formula Cd_5Ni and CdNi, respectively [8, 74]. Hence, if there exists an intermediate layer, it should be composed of these phases [1, 5, 74]. By comparing ALSV of dissolution of a single layer of the alloy with the ALSV of dissolution of the two-layer electrodeposit (Cd–Ni alloy layer with Cd layer on top of it), it was possible to detect an intermediate layer between these two layers. An example is shown in Fig. 7.41. Curve 1 represents the ALSV of the alloy dissolution without the Cd layer on top, curve 2 the ALSV of pure Cd dissolution, while curve 3 represents the ALSV of the two-layer electrodeposit dissolution. As can be seen, curves 1 and 3 are different, with the peaks of β and γ phases dissolution being somewhat higher on the curve 3, while the peak of pure Cd dissolution did not change. As the content of Ni in the alloy layer increased, the difference between these two ALSV curves became smaller.

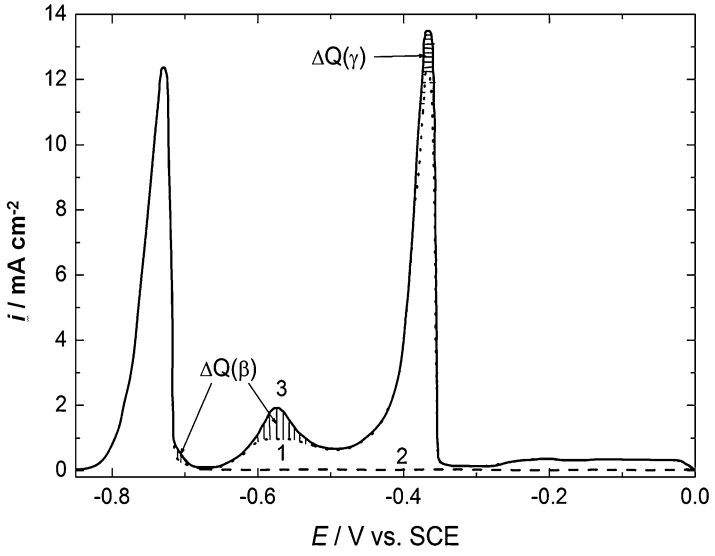

Fig. 7.41 The example of the ALSVs of Cd–Ni alloy dissolution (*dotted line*, *1*), pure Cd dissolution (*dashed line*, *2*), and dissolution of a two-layer electrodeposit (*solid line*, *3*) composed of a layer of Cd–Ni alloy and a layer of pure Cd electrodeposited on top of a layer of the alloy (Reprinted from Ref. [5] with kind permission from Springer)

Hence, the difference between curves 3 and 1 (shaded areas in Fig. 7.41) should represent the intermediate layer. By integration of the surface of shaded areas, it was possible to obtain the charges (amounts) corresponding to the increase of β and γ phases in the two-layer electrodeposit (marked in the figure as $\Delta Q(\beta)$ and $\Delta Q(\gamma)$), which should be a consequence of the formation of an intermediate layer between a layer of alloy and a layer of pure Cd. Thus, the intermediate layer is mainly composed of β and γ phases, which is in good agreement with the theory of an intermediate layer in laminar metal structures [56].

These investigations were performed with the two-layer electrodeposits obtained from two different baths (as stated above). The recorded charges $\Delta Q(\beta)$ and $\Delta Q(\gamma)$, obtained for both investigated baths for alloy electrodeposition, are shown in Fig. 7.42 as a function of the alloy layer composition. As can be seen in the figure, the intermediate layer composition is slightly different in the two cases. The amount of the β phase in the intermediate layer is seen to reach its maximum value at about the same alloy composition (30–40 at.% Ni) in both cases, while the contribution of the γ phase in the intermediate layer was different in two-layer electrodeposits obtained from different baths. Such a behavior clearly indicates that the composition of an intermediate layer is sensitive to the composition of the electroplating bath, since the conditions of electrodeposition were identical in both cases [5, 74].

Assuming that both phases are homogeneously distributed in the intermediate layer, the intermediate layer thickness can be calculated from the charges recorded on the ALSVs. From the formula of the β phase (Cd_5Ni), one can determine the charge corresponding to Ni as 0.167 and to Cd as 0.833 of the total charge $\Delta Q(\beta)$

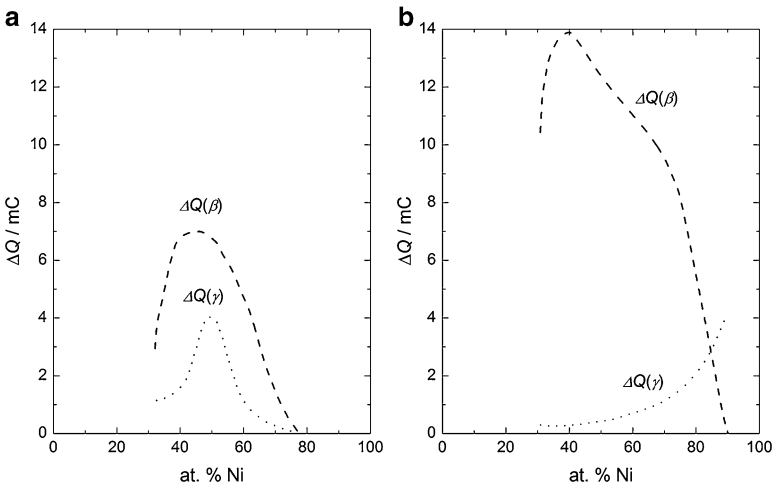

Fig. 7.42 The charges corresponding to the contribution of the β and the γ phases in the intermediate layer obtained by the analysis of the ALSVs of two-layer electrodeposits dissolution. Alloys were electrodeposited from the solutions containing: (**a**) 2 M $NiSO_4$ + 0.2 M $Na_3C_6H_5O_7$ + 0.002 M $CdSO_4$; (**b**) 2 M $Ni(NH_2SO_3)_2$ + 0.5 M H_3BO_3 + 0.002 M $CdSO_4$ (Reprinted from Ref. [5] with kind permission from Springer)

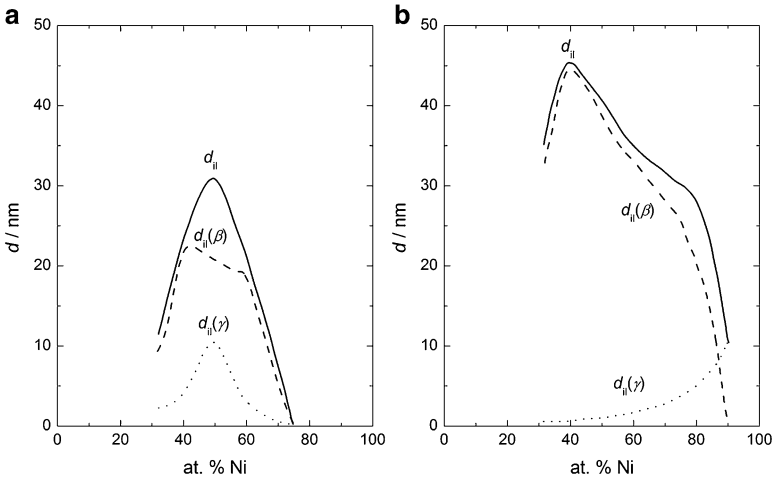

Fig. 7.43 The thickness of the individual phases, $d_{il}(\beta)$ and $d_{il}(\gamma)$, and the intermediate layer, d_{il}, obtained by the analysis of the results presented in Fig. 7.42. (**a**) Samples electrodeposited from the solution 2 M $NiSO_4$ + 0.2 M $Na_3C_6H_5O_7$ + 0.002 M $CdSO_4$; (**b**) Samples electrodeposited from the solution 2 M $Ni(NH_2SO_3)_2$+ 0.5 M H_3BO_3 + 0.002 M $CdSO_4$ (Reprinted from Ref. [5] with kind permission from Springer)

and in a similar way for the γ phase (Ni 0.5 and Cd 0.5 of $\Delta Q(\gamma)$). Using these charges and corresponding values of the density and molecular weights of the two metals, the thicknesses of β and γ phases in the intermediate layer can be calculated. Hence, the total thickness of the intermediate layer should represent the sum of the thickness of individual phases. Figure 7.43 shows the dependence of the thickness of β and γ phases and the total thickness of an intermediate layer (d_{il}) as a function of alloy composition, obtained by the analysis of the results presented in Fig. 7.42. As can be seen, the thickness of the intermediate layer depends on the solution for alloy electrodeposition and its maximum value is about 45 nm. Hence, in certain systems, it is possible to estimate the thickness and the surface of intermediate layer by the application of ALSV technique [5, 74].

7.3.2.4 Mechanical and Magnetic Properties of Multilayered Structures

Mechanical properties of multilayered structures were only investigated for electrodeposits containing Cu/Cu–Ni layers. Following mechanical properties were mainly investigated: Young's modulus [58], hardness [75], and tensile strength [67, 75–77]. It was shown that all investigated properties depend on the thickness of the individual layers and that in all cases multilayered structures showed better properties than that of pure metals and/or their alloys.

The results of hardness investigation [75] are presented in Fig. 7.44. As can be seen, maximum hardness for the electrodeposit containing Cu/Ni-100 layers was

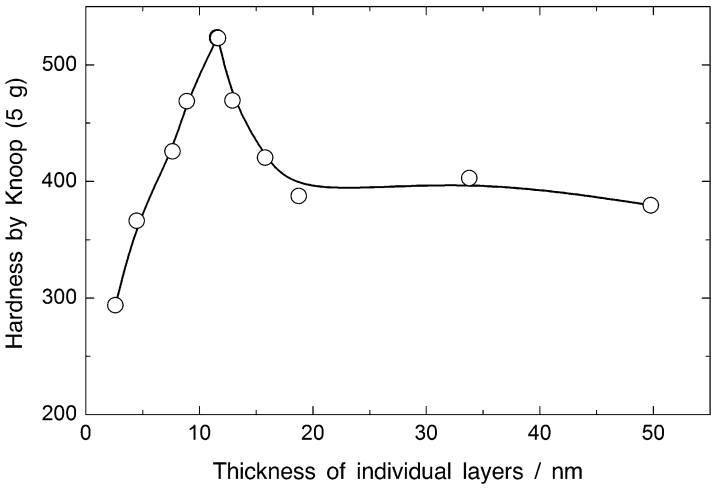

Fig. 7.44 The hardness of the electrodeposit containing Cu/Ni-100 layers as a function of the thickness of individual layers (Reprinted from Ref. [5] with kind permission from Springer)

achieved at the thickness of individual layers of 12 nm. These results are not in agreement with those detected for evaporated layers Cu/Ni-111 [76], where the maximum hardness was obtained for individual layer thickness of 1.6 nm, indicating that, most probably, the hardness depends on the thickness and the total surface area of the intermediate layer which is different for different techniques of multilayered structure formation.

In several investigations, the influence of the individual layer thickness on the tensile strength was reported [66, 75–77]. The results of these investigations are presented in Fig. 7.45. Significant difference in the obtained results is mainly the consequence of different parameters of the electrodeposition process (bath composition, pulse regimes, temperature, etc.). A common explanation for the decrease of tensile strength with the increase of individual layer thickness (after the maximum value) is the increase of the coherence of the intermediate layer. It is concluded that with the decrease of the number of dislocations in the intermediate layer, the probability of their transfer from it to previous or subsequent layer increases, resulting in the decrease of tensile strength.

The dependence of the tensile properties of multilayered Cu-(Ni–Cu) electrodeposits, with the nominal overall composition 90 at.% Ni–10 at.% Cu, was investigated in the work of Tench et al. [68] as a function of the Cu layer thickness (varying from 1 to 15 nm). Multilayers of the nominal thickness of about 50 μm were electrodeposited from a commercial sulfamate bath with the addition of 5 mM $CuSO_4$. Pure Cu layers were plated at −0.14 V versus SCE with cathode rotation at RPM = 750, while Ni layers (with 0.8 at.% Cu) were plated at $i = -105$ mA cm^{-2} from the stagnant bath. The results of the tensile property (ultimate tensile strength, UTS, yield strength, YS, modulus, and strain) measurements are presented in Table 7.5. Considering X-ray data, it was concluded that a decrease in the enhanced strength for such electrodeposits, producing peak at a Cu

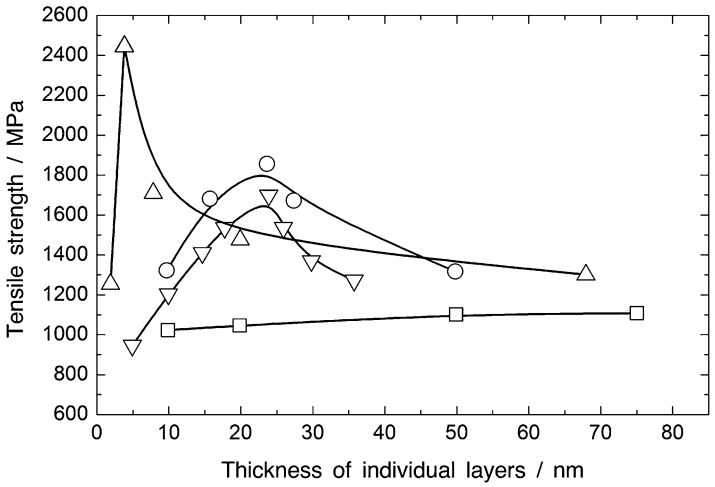

Fig. 7.45 The tensile strength of the multilayered electrodeposits as a function of the thickness of individual layers: ○ – Ref. [67], □ – Ref. [77], Δ – Ref. [78], ▽ – Ref. [68] (Reprinted from Ref. [5] with kind permission from Springer)

Table 7.5 Tensile test for electrodeposited 90 % Ni–10 % Cu multilayers versus Cu layer thickness

Cu layers (nm)	UTS (MPa)	YS (MPa)	Modulus (GPa)	Strain (%)
1.0	1021	795	160	2.4
2.0	1056	840	152	2.4
2.0	1029	881	141	1.4
5.0	1107	893	147	2.0
7.5	1116	844	154	2.1
7.5	1116	848	151	2.7
10.0	1069	807	145	2.8
12.5	978	789	154	1.5
15.0	863	724	130	1.2
		Averages	**148 (±18)**	**2.1 (±0.9)**

Reprinted from Ref. [5] with kind permission from Springer

layer thickness of about 7 nm, is associated with a decrease in the electrodeposit (100) texture (normally established for Ni layers) and an increase in the (110) orientation preferred for Cu deposits.

Concerning the magnetic properties, giant magnetoresistance (GMR), which is significant decrease of electric resistance in the presence of magnetic field, characteristic effect for multilayered structures, has been discovered in 1988 for the systems Fe/Cr/Fe and Fe/Cr by Grünberg and Fert (these scientists received Nobel Prize for physics in 2007). This phenomenon has also been recognized for electrodeposited multilayered structures [79–83]. The strongest effect is detected for multilayered Co–Cu/Cu [81] and Co–Ni–Cu/Cu [82, 83] structures, while less

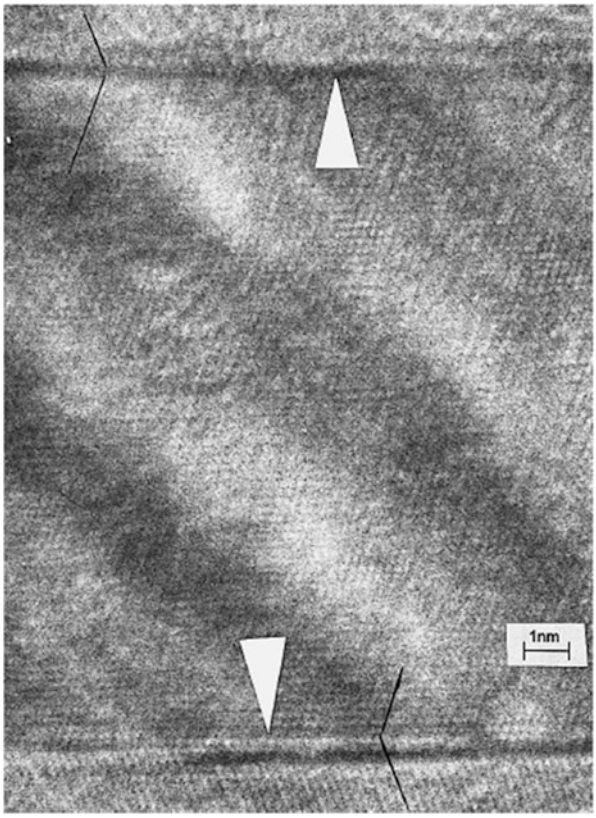

Fig. 7.46 HRTEM picture taken on the Ni–Cu(3.8 nm)/Cu(1.4 nm) sample which shows the atomic structure of a twin boundary (indicated by the *arrow*) and the magnetic/nonmagnetic layers (Reprinted from Ref. [5] with kind permission from Springer)

pronounced effect is detected for the multilayered Ni–Cu/Cu [81] structures. It is important to note that the presence of the intermediate layer of the thickness of 2–3 nm has been detected for the first time by high-resolution transmission electron microscopy (HRTEM) for the multilayered Ni–Cu/Cu structures [79], as shown in Fig. 7.46.

7.3.2.5 Multilayered Structures for Packaging Optoelectronic and Microelectronic Devices

Plating experiments for Au–Sn coatings were carried out from the same solution as in Ref. [53] on pieces sectioned from either metallized AlN (75×75 mm^2) or Si (100 mm diameter) substrates [84]. Examination of the Sn content versus current density revealed that there are two composition plateaus, one at current densities

less than ~1.0 mA cm^{-2} and one at current densities greater than ~2.0 mA cm^{-2}. The former corresponds to a specific Au–Sn intermediate phase, disordered Au_5Sn (ζ), while the latter corresponds to the intermediate phase AuSn (δ) [85]. By utilization of two pulses, one at −0.8 mA cm^{-2} and one at −2.4 mA cm^{-2}, a multilayered structure presented in Fig. 7.47 has been obtained. The duty cycle for each pulse was maintained at 20 % (2 ms on and 8 ms off), but the duration for plating of each phase was varied to yield the desired composition. The plating times for layers shown in Fig. 7.47a were 20 min for −0.8 mA cm^{-2} and 5 min for −2.4 mA cm^{-2}.

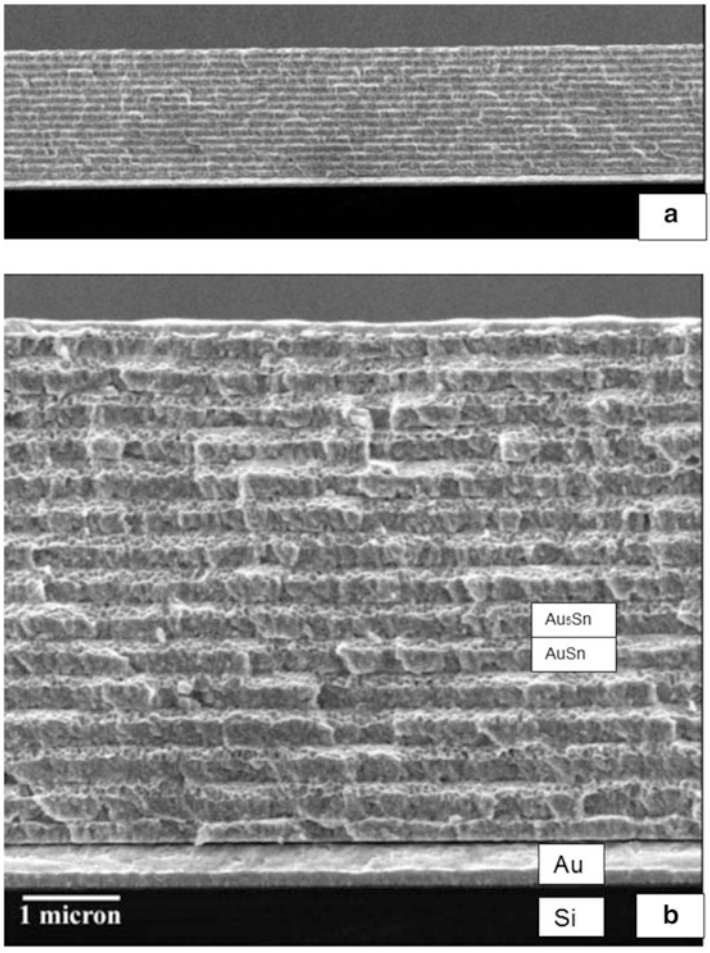

Fig. 7.47 Cross-sectional SEM (SE) images of multilayered electrodeposit at low (**a**) and higher magnification (**b**) (Reprinted from Ref. [85] with kind permission from Springer)

References

1. Despić AR, Jović VD (1995) Electrochemical deposition and dissolution of alloys and metal composites – fundamental aspects. In: White RE, Bockris JO'M, Conway BE (eds) Modern aspects of electrochemistry, vol 27. Plenum Press, New York, pp 143–232
2. Srivastava RD, Mukerjee RC (1976) Electrodeposition of binary alloys: an account of recent developments. J Appl Electrochem 6:321–331
3. Brenner A (1963) Electrodeposition of alloys: principle and practice. Academic, New York
4. Bondar VV, V. Grimina V, Pavlov VN (1980) Itogi nauki i tehniki, Elektrokhimiya, vol 16. Izd. Viniti, Moscow
5. Jović VD, Lačnjevac UČ, Jović BM (2014) Electrodeposition and characterization of alloys and composite materials. In: Djokić SS (ed) Modern aspects of electrochemistry, vol 57. Springer, New York/Heidelberg/Dodrecht/London, pp 1–84
6. Lačnjevac U, Jović BM, Jović VD (2012) Electrodeposition of Ni, Sn and Ni-Sn alloy coatings from pyrophosphate-glycine bath. J Electrochem Soc 159:D310–D318
7. Weast RC (ed) (1976–1977) Handbook of chemistry and physics, 57th edn. CRC Press Inc., Cleveland, pp D141–D146
8. Jović VD, Tošić N (1998) Qualitative and quantitative assessment of phases in electrodeposited Ni + Cd alloys by the ALSV technique. J Electroanal Chem 441:69–76
9. Daen JA (ed) (1999) Lange's handbook of chemistry, 15th edn. McGraw-Hill Inc., New York, pp 920–927
10. Duffield JR, Williams DR, Kron I (1991) Speciation studies of the solubility and aqueous solution chemistry of tin(II)- and tin(IV)-pyrophosphate complexes. Polyhedron 10:377–387
11. Han C, Liu Q, Ivey DG (2008) Kinetics of Sn electrodeposition from Sn(II)-citrate solutions. Electrochim Acta 53:8332–8340
12. Jović VD, Lačnjevac U, Jović BM, Karanović LJ, Krstajić NV (2012) Ni-Sn coatings as cathodes for hydrogen evolution in alkaline solution. Chemical composition, phase composition and morphology effects. Int J Hydrogen Energy 37:17882–17891
13. Dobrovolska TS, Krastev I, Jović BM, Jović VD, Beck G, Lačnjevac U, Zielonka A (2011) Phase identification in electrodeposited Ag-Cd alloys by anodic linear sweep voltammetry and X-ray diffraction techniques. Electrochim Acta 56:4344–4350
14. Dobrovolska TS, Krastev I, Zielonka A (2010) Pattern formation in electrodeposited Silver-Cadmium alloys. ECS Trans 25:1–9
15. Delahay P (1954) New instrumental methods in electrochemistry. Interscience, New York
16. Jović VD, Stojanović MV, Jović BM, Gajić-Krstajić LJ (1992) Electrochemical deposition of Ag, Pd and Ag-Pd alloy from chloride containing electrolyte. J Serb Chem Soc 57:951
17. Sturzenegger B, Puippe JC (1984) Electrodeposition of Palladium-Silver alloys from ammoniacal electrolytes. Plat Met Rev 3:117–124
18. Nakano H, Oue S, Uranka M, Masuda M, Fukushima H, Saka Y, Sawada S, Hattori Y (2010) Electrodeposition of Sn-Ag alloys and evaluation of connection reliability for automotive connectors. Mater Trans 51:712–719
19. Jović VD, Tošić N, Stojanović M (1997) Characterization of electrodeposited Co + Ni alloys by application of the ALSV technique. J Electroanal Chem 420:43–51
20. Dahms H, Croll J (1965) The anomalous codeposition of iron-nickel alloys. J Electrochem Soc 112:771–775
21. Higashi K, Fukushima H, Urakawa T, Adaniya T, Matsuko K (1981) Mechanism of the electrodeposition of zinc alloys containing a small amount of cobalt. J Electrochem Soc 128:2081–2085
22. Horkans T (1979) On the role of buffers and anions in NiFe electrodeposition. J Electrochem Soc 126:1861–1867
23. Horkans T (1981) Effect of plating parameters on electrodeposited NiFe. J Electrochem Soc 128:45–49

24. Wang L, Gao Y, Xue Q, Lui H, Xu T (2005) Microstructure and tribological properties of electrodeposited Ni-Co alloy deposits. Appl Surf Sci 242:326–332
25. Wu BYC, Ferreira PJ, Schuh CA (2005) Nanostructured Ni-Co alloys with tailorable grain size and twin density. Metall Mater Trans A 36A:1927–1936
26. Kanagasabapathy M, Jayakrishnan S (2011) Textural and morphological studies on zinc-iron alloy electrodeposits. J Chem Sci 123:357–364
27. Abdel-Karim R, Reda Y, Muhammed M, El-Raghy S, Shoeib M, Ahmed H (2011) Electrodeposition and characterization of nanocrystalline Ni-Fe alloys. J Nanomater 2011:1–8
28. Podlaha EJ, Landolt D (1996) Induced codeposition I. An experimental investigation of Ni-Mo alloys. J Electrochem Soc 143:885–892
29. Podlaha EJ, Landolt D (1996) Induced codeposition II. A mathematical model describing the electrodeposition of Ni-Mo alloys. J Electrochem Soc 143:893–899
30. Podlaha EJ, Landolt D (1997) Induced codeposition III. Molybdenum alloys with nickel, cobalt, and iron. J Electrochem Soc 144:1672–1680
31. Marlot A, Kern P, Landolt D (2002) Pulse plating of Ni-Mo alloys from Ni-rich electrolytes. Electrochim Acta 48:29–36
32. Zeng Y, Li Z, Ma M, Zhou S (2000) In situ surface Raman study of the induced codeposition mechanism of Ni-Mo alloys. Electrochem Comm 2:36–38
33. Sanches LS, Domingues SH, Carubelli A, Mascaro LH (2003) Electrodeposition of Ni-Mo and Fe-Mo alloys from sulfate-citrate acid solutions. J Braz Chem Soc 14:556–563
34. Jović VD, Jović BM, Lačnjevac U, Branković G, Bernik S, Rečnik A (2010) An attempt to predict the mechanism of Mo-Ni-O powders electrodeposition from the results of their TEM analysis. Electrochim Acta 55:4188–4193
35. Sanches L, Domingues SH, Marino CEB, Mascaro LH (2004) Characterization of electrochemically deposited Ni-Mo alloy coatings. Electrochem Comm 6:543–548
36. Krstajić NV, Jović VD, Gajić-Krstajić LJ, Jović BM, Antozzi AL, Martelli GN (2008) Electrodeposition of Ni-Mo alloy coatings and their characterization as cathodes for hydrogen evolution in sodium hydroxide solution. Int J Hydrogen Energy 33:3676–3687
37. Grgur BN, Krstajić NV, Elezović N, Jović VD (2005) Electrodeposition and characterization of Fe-Mo alloys as cathodes for hydrogen evolution in the process of chlorate production. J Serb Chrem Soc 70:879–889
38. Elezović NR, Jović VD, Krstajić NV (2005) Kinetics of the hydrogen evolution reaction on Fe-Mo film deposited on mild steel support in alkaline solution. Electrochim Acta 50:5594–5601
39. Jović V, Elezović N (2009) Electrochemical deposition and characterization of alloys. Institute for Multidisciplinary Research University of Belgrade, Belgrade, pp 1–101
40. Krastev I, Dobrovolska TS (2013) Pattern formation during electrodeposition of alloys. J Solid State Electrochem 17:481–488
41. Wojtowicz J (1972) Oscillatory behavior in electrochemical systems. In: Bockris JO'M, Conway B (eds) Modern aspects of electrochemistry, vol 8. Butterworths, London, pp 47–115
42. Krischer K (2001) Spontaneous formation of spatiotemporal patterns at the electrode|electrolyte interface. J Electroanal Chem 501:1–21
43. Koper MTM (1996) Oscillations and complex dynamical bifurcations in electrochemical systems. In: Prigogine I, Rice SA (eds) Advances in chemical physics, vol 92. Wiley, Hoboken, pp 161–298
44. Raub E (1953) Galvanische Legierungsniederschläge. Metalloberfläche 7:A17–A27
45. Krastev I, Baumgärtner ME, Raub CJ (1992) Stromoszillationen bei der galvanischen Abscheidung Untersuchungen zur Silber-Antimon-Legierungsabscheidung, Teil 2. Metalloberfläche 46:115–120
46. Hrussanova A, Krastev I, Beck G, Zielonka A (2010) Properties of silver-tin alloys obtained from pyrophosphate-cyanide electrolytes containing EDTA salts. J Appl Electrochem 40:2145–2151

47. Krastev I, Baumgärtner ME, Raub CJ (1992) Stromoszillationen bei der galvanischen Abscheidung. Untersuchungen zur Silber-Antimon-Legierungsabscheidung. Teil 1. Metalloberfläche 46:63–66
48. Raub E, Schall A (1938) Silber-Indium-Legierungen. Ein beitrag zur frage der anlaufbeständigen Silber legierungen. Zeitschr Metallkunde 30:149–151
49. Kristev I, Nikolova M (1986) Structural effects during the electrodeposition of silver-antimony alloys from ferrocyanidethiocyanate electrolytes. J Appl Electrochem 16:875–878
50. Kristev I, Nikolova M (1986) Phase composition and structure of silver–antimony alloy deposits plated from ferrocyanidethiocyanate electrolytes. J Appl Electrochem 16:867–874
51. Krastev I, Dobrovolska T, Lacnjevac U, Nineva S (2012) Pattern formation during electrodeposition of indium-cobalt alloys. J Solid State Electrochem 16:3449–3456
52. Nakabayashi S, Krastev I, Aogaki R, Inokuma K (1998) Electrochemical instability of Ag/Sb co-deposition coupled with a magnetohydrodynamic flow. Chem Phys Lett 294:204–208
53. Sun W, Ivey DG (1999) Development of an electroplating solution for codepositing Au-Sn alloys. Mater Sci Eng B 65:111–122
54. Sun W, Ivey DG (2001) Microstructural study of co-electroplated Au/Sn alloys. J Mater Sci 36:757–766
55. Bradley PE, Landolt D (1999) Pulse-plating of copper-cobalt alloys. Electrochim Acta 45:1077–1087
56. Metcalfe AG (1974) Interfaces in metal composites. Academic, New York, pp 65–102
57. Cohen U, Koch FB, Sard R (1983) Electroplating of Cyclic Multilayered Alloy (CMA) coatings. J Electrochem Soc 130:1987–1995
58. Tench D, White J (1984) Enhanced tensile strength for electrodeposited nickel-copper multilayer composites. Metall Trans 15A:2039–2040
59. Ogden C (1986) High-strength, composite Copper-Nickel electrodeposits. Plat Surf Finish 73:130–134
60. Verbruge MW, Tobias CW (1985) A mathematical model for the periodic electrodeposition of multicomponent alloys. J Electrochem Soc 132:1298–1307
61. Despić AR, Jović VD (1987) Electrochemical formation of laminar deposits of controlled structure and composition: I. Single current pulse galvanostatic technique. J Electrochem Soc 134:3004–3011
62. Despić AR, Jović VD, Spaić S (1989) Electrochemical formation of laminar deposits of controlled structure and composition: II. Dual current pulse galvanostatic technique. J Electrochem Soc 136:1651–1657
63. Despić AR, Trišović T (1993) Transition layer thickness in microlaminar deposits. J Appl Electrochem 23:662–668
64. Power CP, Ritchie IM (1975). In: Conway BE, Bockris JO'M (eds) Modern aspects of electrochemistry, Metal displacement reactions, vol. 11, Plenum Press, New York, pp 199–250
65. Yahalom J, Zadok O (1987) Formation of composition-modulated alloys by electrodeposition. J Mater Sci 22:499–503
66. Lashmore DS, Dariel MP (1988) Electrodeposited Cu-Ni textured superlattices. J Electrochem Soc 135:1218–1221
67. Tench DM, White JD (1990) Considerations in electrodeposition of compositionally modulated alloys. J Electrochem Soc 137:3061–3066
68. Tench M, White J (1991) Tensile properties of nanostructured Ni-Cu multilayered materials prepared by electrodeposition. J Electrochem Soc 138:3757–3758
69. Ebrahimi F, Liscano AJ (2001) Microstructure/mechanical properties relationship in electrodeposited Ni/Cu nanolaminates. Mater Sci Eng A301:23–34
70. Yang C-C, Cheh HY (1995) Pulsed electrodeposition of copper/nickel multilayers on a rotating disk electrode: I. Galvanostatic deposition. J Electrochem Soc 142:3034–3040
71. Yang C-C, Cheh HY (1995) Pulsed electrodeposition of copper/nickel multilayers on a rotating disk electrode: II. Potentiostatic deposition. J Electrochem Soc 142:3040–3043

72. Roy S, Landolt D (1995) Effect of off-time on the composition of pulse-plated Cu-Ni alloys. J Electrochem Soc 142:3021–3027
73. Bradley PE, Landolt D (1997) A surface coverage model for pulse-plating of binary alloys exhibiting a displacement reaction. Electrochim Acta 42:993–1003
74. Despić AR, Jović VD, Tošić N (1998) Intermediate layers in electrodeposited CMA coatings. Surf Coat Techn 105:206–212
75. Oberle RR, Cammarata RC (1995) Dependence of hardness on modulation amplitude in electrodeposited Cu-Ni compositionally modulated thin films. Scr Metall Et Mater 32:583–588
76. Cammarata RC, Schleisinger TE, Kim C, Qadri SB, Edelstein AS (1990) Nanoindentation study of the mechanical properties of copper-nickel multilayered thin films. Appl Phys Lett 56:1862–1864
77. Meneyes S, Anderson DP (1990) Wavelength-property correlation in electrodeposited ultrastructured Cu-Ni multilayers. J Electrochem Soc 137:440–444
78. Simunovich D, Schleisinger M, Snyder DD (1994) Electrochemically layered Copper-Nickel nanocomposites with enhanced hardness. J Electrochem Soc 141:L10–L11
79. Cziraki A, Pierron-Bohnes V, Ulhaq-Bouillet C, Toth-Kadar E, Bakonyi I (1998) A cross-section high-resolution transmission electron microscopy study of electrodeposited Ni-Cu/Cu multilayers. Thin Solid Films 318:239–242
80. Bakonyi I, Toth-Kadar E, Becsei T, Toth J, Tarnoczi T, Cziraki A, Geröcs I, Nabiyouni G, Schwarzacher W (1996) Giant magnetoresistance in self-supporting electrodeposited Ni-Cu/Cu multilayers. J Magn Magn Mater 156:347–349
81. Bird KD, Schleisinger M (1995) Giant magnetoresistance in electrodeposited Ni/Cu and Co/Cu multilayers. J Electrochem Soc 142:L65–L66
82. Hart R, Alper M, Attenborough K, Schwarzacher W (1994). In: Romankiw LT, Herman DAJr (eds) Proc. 3rd int. symp. on magnetic mater. processes and devices, electrodeposition division of the electrochem. soc, vol. 94–96, Pennington, p 215
83. Hua SZ, Lashmore DS, Salamanca-Riba L, Schwarzacher W, Swartzendruber LJ, McMichael RD, Bennett LH, Hart R (1994) Giant magnetoresistance peaks in CoNiCu/Cu multilayers grown by electrodeposition. J Appl Phys 76:6519–6521
84. He A, Djurfos B, Akhlaghi S, Ivey DG (2002) Pulse plating of gold-tin alloys for microelectronic and optoelectronic devices. Plat Surf Finish 89:48–53
85. Djurfos B, Ivey DG (2001) Pulsed electrodeposition of the eutectic Au/Sn solder for optoelectronic packaging. J Electron Mater 30:1249–1254